



**SCUOLA INTERNAZIONALE  
SUPERIORE di STUDI AVANZATI**  
International School  
for Advanced Studies

## Interplay of Superconductivity and Magnetism in the Two Dimensional Kondo Lattice Model

**Candidate:**  
Mohammad Zhian Asadzadeh

**Advisors:**  
Dr. Federico Becca  
Prof. Michele Fabrizio

Thesis submitted for the Degree of Doctor of Philosophiæ  
November/2013

**This thesis is dedicated to my parents.**  
for their endless love, support and encouragement

# Abstract

Since the original discovery of heavy fermion behavior in the late seventies by Andres *et al.* [1], heavy fermions keep attracting scientific interest due to their exotic and unusual properties. These are inter-metallic compounds that contain rare earth elements, like cerium, praseodymium, and ytterbium, and actinides like uranium. The term “heavy” refers to their large effective electronic mass, as large as 1000 times the normal metal ones. The active physics in these materials results from the magnetic moments, associated to the partially filled  $f$ -shells of rare earth or actinide ions, being immersed into a quantum sea of mobile conduction electrons. In most rare earth metals and insulators, local moments tend to order magnetically, but in heavy electron metals the quantum mechanical jiggling of the local moments induced by delocalized electrons is fierce enough to melt magnetic order. The mechanism by which this takes place involves a remarkable piece of quantum physics known as the “Kondo effect” [2] that describes the process by which a magnetic impurity get screened by conduction electrons, forming the so-called Kondo singlet below a characteristic temperature/energy scale named the Kondo temperature,  $T_K$ . Even though the Kondo effect refers strictly speaking to a very dilute concentration of magnetic ions, typically few part per million, the same physics is believed to play a role in heavy fermions.

Heavy fermion materials have become recently popular also in the study of the quantum critical behavior of matter in the vicinity of a zero temperature second-order phase transition. Indeed, heavy fermions realize prototypical examples of quantum critical points that separate at zero temperature magnetic and paramagnetic phases. Experimentally, quantum critical points are attained by tuning non-thermal control parameters, such as pressure, chemical doping or applied magnetic field, so as to drive continuously to zero the magnetic ordering temperature.

One of presently lively discussions up to date is about the appearance of two types of magnetic quantum critical points, depending on the behavior of the Kondo singlet as the transition is approached from paramagnetic side. If the Kondo singlet remains across the magnetic transition, the latter is of a spin-density-wave type in which the only critical degrees of freedom are the fluctuations of the magnetic order parameter. In this scenario, the Fermi volume does not change and contains both  $f$  and conduction electrons.

The alternative scenario invokes instead a local quantum criticality, where the Kondo singlet breaks down right at the magnetic transition, bringing about novel critical modes. Across such a quantum critical point, one expects a sudden collapse of the large Fermi surface of the paramagnetic side to a small magnetic one that contains only conduction electrons.

Around a quantum critical point interesting phenomena such as non-Fermi liquid behavior or the appearance of exotic phases may appear. Indeed, many heavy fermions show superconductivity right after the magnetic transition. There are also evidences of coexisting magnetism and superconductivity [3]. Emergence of superconductivity in heavy fermions is at first glance quite surprising, since in the conventional wisdom magnetic impurity scattering is pair-breaking. The evidence of non- $s$  wave symmetry of the order parameter brings these materials in the class of unconventional superconductors, where pairing is not phonon-mediated but likely caused by magnetic fluctuations. This issue has attracted a lot of experimental and theoretical interest.

From the theoretical point of view, already building up a microscopic Hamiltonian that could capture the main physics and reproduce the phase diagram of heavy fermions is a challenge that is still ongoing. One of the first attempts to attack this issue was done by Anderson, [4] who proposed in 1961 the model that is nowadays universally known as the Anderson impurity model. Later on, Doniach [5] introduced a lattice version believed to describe heavy fermions, the so-called Kondo lattice model. The latter one has been studied extensively and there is a strong belief that it indeed captures the basic physics of heavy fermions.

In one dimension the Kondo lattice model has been widely studied and its phase diagram is well established (for a comprehensible review see Ref.[6]). Here, there are only three phases at zero temperature: the Kondo insulator at the compensated regime (i.e., when the number of itinerant electron equals the number of localized spins) and two metallic phases, one ferromagnetic and another paramagnetic [7, 8]. Most importantly, there is evidence that the standard Kondo lattice model does not present superconducting tendencies close to the compensated regime [9]. In two dimensions, an earlier work by Lacroix et al. [10] showed the evidence of an antiferromagnetic phase close to the compensated regime and for small Kondo exchange couplings. Indeed, the two-dimensional Kondo lattice model also includes antiferromagnetism which, at the compensated regime, is continuously connected to the spin-gapped insulator [11]. There are Monte Carlo results [11, 12] as well as series expansion around the strong coupling limit [13] that support the existence of a critical point. Recently, motivated by Hall coefficient experiments [14] the nature of the quantum critical point has attracted a lot of interest. It has been confirmed by several works [15, 16, 17, 18] that there are two kinds of phase transition: an antiferromagnetic one and a topological one

(where a Fermi surface reconstruction takes place). Therefore, there are two types of magnetic phases based on the topology of the Fermi surface, which may be electron like (AFe) or hole like (AFh). Regarding superconductivity, density-matrix renormalization group calculations suggested that the standard Kondo lattice model does not support a superconducting ground state [9], while robust  $d$ -wave pairing correlations have been reported in the Kondo-Heisenberg model [19]. Recent Hartree-Fock calculations also suggested the existence of  $d$ -wave pairing in the two-dimensional Kondo-Heisenberg model in the non-magnetic sector [20].

In this Thesis we study the ground-state phase diagram of various versions of the Kondo lattice model in two dimensions, starting from the simplest Doniach's one, with special focus on the possible appearance of superconductivity in the phase diagram. To attack this problem, we adopt a variational Monte Carlo scheme that allows treating quite large lattices, thus going beyond the one-dimensional and, at the opposite, the infinite-dimensional cases where most of the numerical studies have been restricted so far.

Using Gutzwiller projected wave functions we are able to satisfy the local constraint of one electron per  $f$  orbital locally not in average: this is the main advantage of the variational Monte Carlo against the mean-field approach. The flexibility of this variational method makes it possible to account for different types of correlations (specially pairing correlations) in the trial wave function, which are not present at the mean-field level. A full optimization of the variational wave function allows us to finally depict the phase diagram.

## Main blocks of the thesis

This thesis is divided in five chapters:

★ In chapter (1), we briefly study the heavy-fermion terminology. We start by introducing heavy fermions and their properties and then we discuss simple microscopic models that may capture the basic physics of these strongly-correlated materials. We discuss the quantum critical behavior and its consequences including Fermi surface reconstruction, non-Fermi liquid behavior, and the appearance of superconductivity in the proximity of a magnetic transition.

★ In chapter (2), we introduce the methods that we have used in this thesis. First we briefly introduce the Hartree-Fock method and the procedure to setting up the self-

consistent equations. Then, we introduce the variational Monte Carlo technique and the stochastic reconfiguration algorithm for minimizing the variational energy in an efficient way.

★ In chapter (3), we study the Kondo lattice model and establish our best variational phase diagram. In particular, we start by showing the phase diagram obtained by the simple Hartree-Fock mean-field method and then we use the Monte Carlo technique to include relevant correlations inside the variational wave functions. One of the main conclusion is that in the paramagnetic sector there is a large regime with  $d$ -wave superconductivity. However, once magnetic order is allowed in the variational wave function, the final phase diagram does not include any superconducting phase.

★ In chapter (4), we add an additional ingredient to the standard Kondo lattice Hamiltonian. The idea is to frustrate magnetism in order to favor the superconducting phase. In particular, we consider a next-nearest-neighbor hopping for conduction electrons. Surprisingly, we find a huge enhancement in condensation energy and consequently an extension of the superconducting region. Most importantly, even by including magnetism in the variational state, the final phase diagram still contain a superconducting region, in the vicinity of the magnetic transition.

★ In chapter (5), following our quest for superconductivity, we consider the effect of direct Heisenberg interaction term between local spins (in the unfrustrated model). As a result, we find a significant enhancement in the condensation energy, which implies the extension of the superconducting region. Furthermore, we find also a region of coexistence between antiferromagnetism and superconductivity. Finally, we show the phase diagram and discuss the relevance of our results for realistic experimental phase diagram for heavy fermions.

# Contents

<b>Abstract</b>	<b>i</b>
<b>1. Introduction</b>	<b>1</b>
1.1. Heavy fermions . . . . .	1
1.2. From Anderson model to the Kondo model . . . . .	1
1.2.1. The single impurity Anderson model . . . . .	2
1.2.2. Schrieffer Wolff transformation . . . . .	3
1.2.3. The Kondo lattice model . . . . .	4
1.3. Quantum criticality . . . . .	5
1.3.1. Fermi surface collapse and break-down of Kondo effect . . . . .	6
1.3.2. Non-Fermi liquid behavior . . . . .	7
1.3.3. Heavy fermion superconductivity . . . . .	9
<b>2. Methods</b>	<b>13</b>
2.1. Hartree-Fock mean-field . . . . .	13
2.2. The variational Monte Carlo . . . . .	15
2.3. The minimization algorithm . . . . .	19
<b>3. Kondo Lattice Model on 2D Lattice</b>	<b>25</b>
3.1. Kondo lattice model . . . . .	25
3.2. Hartree-Fock mean field approximation . . . . .	26
3.2.1. Mean-field results . . . . .	30
3.3. Variational Monte Carlo approach . . . . .	31
3.3.1. Variational Monte Carlo results . . . . .	34
3.4. Spectral function and Fermi surface topology . . . . .	40
3.5. Why Fermi surface reconstruction? . . . . .	41
3.6. Conclusion . . . . .	45
<b>4. Frustrated Kondo Lattice Model on 2D Lattice</b>	<b>47</b>
4.1. The frustrated model and basic considerations . . . . .	48
4.2. Positive next-nearest-neighbor hopping amplitude . . . . .	50

---

4.2.1. Paramagnetic sector . . . . .	50
4.2.2. Antiferromagnetic sector . . . . .	52
4.3. Negative next-nearest-neighbor hopping amplitude . . . . .	54
4.4. Final variational phase diagram and conclusions . . . . .	56
<b>5. Kondo Heisenberg Model on 2D Lattice</b>	<b>59</b>
5.1. Kondo Heisenberg lattice model . . . . .	59
5.2. Paramagnetic sector . . . . .	60
5.3. Antiferromagnetic sector . . . . .	62
5.4. Final phase diagram and conclusions . . . . .	64
<b>6. Summary</b>	<b>67</b>
<b>7. Acknowledgement</b>	<b>69</b>
<b>A. Pair-pair correlations for free fermions on 2D lattice</b>	<b>71</b>
<b>Bibliography</b>	<b>73</b>

# 1. Introduction

## 1.1. Heavy fermions

The term “heavy fermion” was coined by Steglich [21] in the late seventies to describe the electronic excitations in a new class of inter-metallic compounds with an electronic density of states as much as 1000 times larger than copper. The properties of heavy fermion compounds derive from the partially filled  $f$  orbitals [22, 23, 24] of rare earth or actinide ions. The large nuclear charge in these ions causes their  $f$  orbitals to collapse inside the inert gas core of the ion, turning them into localized magnetic moments with definite  $J = L + S$  because of the large spin-orbit coupling. An example of such behavior is provided by the inter-metallic crystal CeCu<sub>6</sub>. Superficially, this material is copper, alloyed with 14% cerium. In this material, at room temperature the  $f$  electrons behave as localized magnetic moments, bounded to the cerium ions. Yet at low temperatures they crossover into mobile electrons, with a very large effective mass. The heavy electrons that develop in this material are a thousand times “heavier” than those in metallic copper, and move with a group velocity that is slower than sound. Unlike copper, which has Fermi temperature of order 10,000K, that of CeCu<sub>6</sub> is of order 10K, and above this temperature, the heavy electrons lose coherence and reveal the underlying magnetic moments of the cerium ions, which manifest themselves as a Curie law susceptibility  $\chi \sim \frac{1}{T}$ . There are many hundreds of different variety of heavy electron materials with many novel and exotic phases at low temperature.

## 1.2. From Anderson model to the Kondo model

In the early 1930’s de Haas et al. [25] in Leiden, discovered a resistance minimum that develops in the resistivity of copper, gold, silver and many other metals at low temperatures. It took a further 30 years before the purity of metals and alloys improved to a point where the resistance minimum could be linked to the presence of magnetic impurities [26, 27]. Clogston et al. [26] found that it was possible to tune the conditions under which Iron impurities in Niobium were magnetic, by alloying with Molybdenum. Beyond a certain concentration of Molybdenum, the Iron impurities become magnetic and a resistance minimum was observed. Naturally, the desire to understand these exciting phenomena sparked interest in the nature and formation of the local moment

of the impurities. Before Anderson [4], impurities in a metallic host were mainly treated as scattering potentials. Friedel [28] had shown in the fifties that such a potential within the conduction band of the host system would lead to highly localized states (“virtual bound” states). Anderson approached the problem from a different direction. He modeled the impurity as a near-atomic state that would hybridize with the states of the host system. By including an on-site Coulomb-interaction term for the impurity he was able to derive a criterion for the local moment formation employing a Hartree-Fock approximation. His model was to become known as the single impurity Anderson model

### 1.2.1. The single impurity Anderson model

We begin with a discussion of how magnetic moments form at high temperatures, and how they are screened at low temperatures to form a Fermi liquid. The basic model for local moment formation which Anderson [4] introduced is

$$H = \sum_{k,\sigma} \epsilon_k n_{k,\sigma} + \sum_{k,\sigma} V(k) \left[ c_{k,\sigma}^\dagger f_\sigma + f_\sigma^\dagger c_{k,\sigma} \right] + E_f n_f + U n_{f\uparrow} n_{f\downarrow}. \quad (1.1)$$

There are two key ingredients in the Anderson model:

#### a) Atomic limit and formation of local moments

The atomic physics of an isolated ion with a single  $f$  state, described by :

$$H_{atomic} = E_f n_f + U n_{f\uparrow} n_{f\downarrow}, \quad (1.2)$$

where  $E_f$  is the energy of the  $f$  state and  $U$  is the Coulomb energy associated with two electrons in the same orbital. The atomic physics contains the basic mechanism for local moment formation, valid for  $f$  electrons, but also seen in a variety of other contexts, such as transition metal oxides and other correlated materials. The four quantum states of the atomic model are

$$\begin{aligned} |f^2\rangle & E(f^2) = 2E_f + U \\ |f^0\rangle & E(f^0) = 0 \\ |f^1 \uparrow\rangle, |f^1 \downarrow\rangle & E(f^1) = E_f. \end{aligned} \quad (1.3)$$

In a magnetic states ( $|f^1 \uparrow\rangle, |f^1 \downarrow\rangle$ ), the cost of removing or adding an electron to the  $f^1$  state is positive, i.e.

$$\text{removing : } E(f^0) - E(f^1) = -E_f > 0 \quad (1.4)$$

$$\text{adding : } E(f^2) - E(f^1) = E_f + U > 0. \quad (1.5)$$

So a local moment is well defined if the temperature is smaller than the valence fluctuation scale

$$T_{VF} = \min(E_f + U, -E_f). \quad (1.6)$$

At lower temperatures, the atom behaves effectively as a spin.

### b) Hybridization

When the magnetic ion is immersed in a sea of itinerant electrons, the  $f$  electrons within the core of the atom hybridize with the Bloch states of surrounding electron sea through [28]:

$$H_{\text{hybridization}} = \sum_{k,\sigma} \epsilon_k n_{k,\sigma} + \sum_{k,\sigma} V(k) \left[ c_{k,\sigma}^\dagger f_\sigma + f_\sigma^\dagger c_{k,\sigma} \right], \quad (1.7)$$

where the hybridization matrix element  $V(k) = \langle k | V_{\text{atomic}} | f \rangle$  is the overlap of the atomic potential between a localized  $f$  state and a Bloch wave. In the absence of any interactions ( $U = 0$ ) the hybridization broadens the localized  $f$  state producing a resonance of width

$$\Delta = \pi \sum_k |V(k)|^2 \delta(\epsilon_k - E_f) \simeq \pi V^2 \rho, \quad (1.8)$$

where  $V$  is the average of hybridization around the Fermi surface and  $\rho$  is the density of states at Fermi level  $\mu$ , and we have assumed that  $|E_f - \mu| \ll \mu$ .

Anderson's original work provided a mean-field treatment of the interaction. He found that for interactions larger than  $U_c \sim \pi \Delta$  local moments develop with a finite magnetization  $M = \langle n_\uparrow \rangle - \langle n_\downarrow \rangle$ . This allows one to explain why some transition metal impurities lost their moments when embedded in a metal, while some others preserved it.

### 1.2.2. Schrieffer Wolff transformation

The unitary or canonical transformation that eliminates the charge fluctuations at scales  $(E_f + U)$  and  $(-E_f)$  was first carried out by Schrieffer and Wolff [29, 30], who showed how the Anderson model gives rise to a residual antiferromagnetic interaction between the local moments and conduction electrons. The emergence of this antiferromagnetic interaction is associated with a process called super-exchange: the virtual process in which an electron or hole briefly migrates off the ion, to be immediately replaced by another with different spin. When these processes are removed by the canonical transformation, they generate an antiferromagnetic interaction between the local moment and the conduction electrons. This can be seen by considering the two possible spin exchange processes

$$e_\uparrow^- + f_\downarrow^1 \leftrightarrow f^2 \leftrightarrow e_\downarrow^- + f_\uparrow^1 \quad \Delta E_1 \sim U + E_f \quad (1.9)$$

$$h_{\downarrow}^{\uparrow} + f_{\downarrow}^{\uparrow} \leftrightarrow f^0 \leftrightarrow h_{\uparrow}^{\uparrow} + f_{\uparrow}^{\uparrow} \quad \Delta E_2 \sim -E_f. \quad (1.10)$$

Both process require the  $f$  electron and incoming particle to be in a spin-singlet state. From second-order perturbation theory, the energy of the singlet is lowered with respect to the triplet by an amount  $J$  where

$$J = 4V^2 \left[ \frac{1}{\Delta E_1} + \frac{1}{\Delta E_2} \right], \quad (1.11)$$

and  $V \sim V(k_f)$  is the hybridization matrix element near the Fermi surface. If we introduce the electron spin density operator  $\sigma^\alpha(0) = \frac{1}{2N} \sum_{k,k',\sigma,\sigma'} c_{k,\sigma}^\dagger \tau_{\sigma,\sigma'}^\alpha c_{k',\sigma'}$  where  $N$  is the number of sites in the lattice and  $\tau^\alpha$  the Pauli matrices, then the effective interaction will have the form

$$H_K = -2JP_{S=0}, \quad (1.12)$$

where  $P_{S=0} = [\frac{1}{4} - \sigma(0) \cdot S]$  is the singlet projection operator,  $S$  being the spin of the localized moment. If we drop the constant term, the the effective interaction induced by the virtual charge fluctuations must have the form

$$H_K = J\sigma(0) \cdot S. \quad (1.13)$$

The complete Kondo model describing the conduction electrons and their interaction with the local moment is:

$$H = \sum_{k,\sigma} \epsilon_k c_{k,\sigma}^\dagger c_{k,\sigma} + J\sigma(0) \cdot S, \quad (1.14)$$

in which the interaction is antiferromagnetic  $J > 0$ .

In Japan, Kondo [2] set out to examine the consequences of this result. He calculated the scattering rate  $1/\tau$  of electrons off a magnetic moment to one order higher than Born approximation, and found the remarkable result that

$$\frac{1}{\tau} \propto (J\rho)^2 + 4(J\rho)^3 \ln \frac{D}{T}, \quad (1.15)$$

where  $\rho$  is the density of state of electrons in the conduction sea and  $D$  is the width of the electron band. As the temperature is lowered, the logarithmic term grows and the scattering rate and resistivity ultimately rises, connecting the resistance minimum with the antiferromagnetic interaction between spins and their surroundings.

### 1.2.3. The Kondo lattice model

After the discovery of the heavy-electron materials, Doniach [5] suggested that the minimal model that may capture the low-energy physics is a straightforward lattice

generalization of the Kondo model of Eq.(1.14), namely the well-known Kondo lattice model:

$$H = \sum_{k,\sigma} \epsilon_k c_{k,\sigma}^\dagger c_{k,\sigma} + J \sum_i S_i \cdot s_i, \quad (1.16)$$

where  $s_i = (s_i^x, s_i^y, s_i^z)$  is the spin operator for the  $c$  electrons on the lattice site  $i$ , i.e.,  $s_i^\alpha = 1/2 \sum_{\sigma,\sigma'} c_{i,\sigma}^\dagger \tau_{\sigma,\sigma'}^\alpha c_{i,\sigma'}$ ,  $\tau^\alpha$  being the Pauli matrices. Similarly,  $S_i = (S_i^x, S_i^y, S_i^z)$  is the spin operator for the localized  $f$  electrons,  $S_i^\alpha = 1/2 \sum_{\sigma,\sigma'} f_{i,\sigma}^\dagger \tau_{\sigma,\sigma'}^\alpha f_{i,\sigma'}$ . By constraint there is one  $f$  electron per each site and the exchange coupling is antiferromagnetic, i.e.,  $J > 0$ . The non-trivial behavior at low temperature emerges from the competition between the hopping term  $t$ , which tends to delocalize  $c$  electrons, and the exchange Kondo coupling  $J$ , which instead leads to singlet formation of  $c$  electrons with  $f$  moments. Moreover, itinerant electrons mediate indirect magnetic interactions among localized  $f$  spins, possibly leading to a true magnetic order at zero temperature. The competition between the Kondo effect and the tendency of generating a long-range magnetic order is at the roots of the so-called quantum phase transitions. As a result of these quantum phase transitions, many interesting phenomena emerge, which we will briefly discuss in the following.

### 1.3. Quantum criticality

Quantum criticality describes the collective fluctuations associated with a second-order phase transition at zero temperature. The point in which this transition happens is called quantum critical point (QCP). A QCP occurs in many body systems as a result of competing interactions that lead to different ground states. QCPs are of great current interest because of their singular ability to influence the finite temperature properties of materials. Recently, heavy-fermion materials have played a key role in the study of antiferromagnetic QCPs.

Many heavy electron systems can be tuned with a non-thermal control parameter such as pressure, chemical doping or applied magnetic field to a point where their antiferromagnetic ordering temperature is driven continuously to zero to produce a QCP [31, 32, 33, 34]. The role of the control parameter is to tune the zero point motion of the constituent particles. In other words, such a parameter controls quantum mechanical tunneling dictated by Heisenberg's uncertainty principle, changing the degree of quantum fluctuations. This is the analog of varying the thermal fluctuations in the case of temperature driven classical phase transition, such as the melting of ice. The generic phase diagram is illustrated in Fig. 1.1, where  $\delta$  represents the tuning parameter.

Around the quantum critical region many interesting phenomena appear which nowadays attract lot of interest. In the following we will briefly mention some of them.

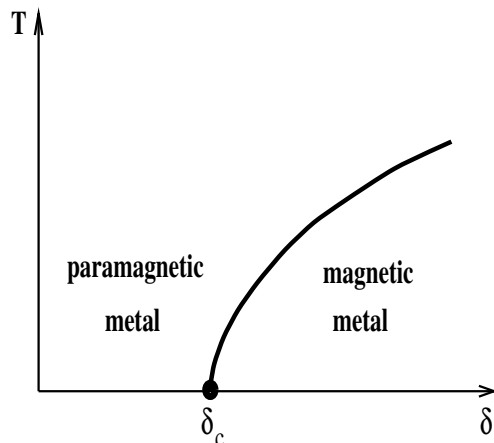


Figure 1.1.: Generic phase diagram of a heavy fermion metal which exhibits a quantum critical point at temperature  $T = 0$  and at a critical value of some tuning parameter,  $\delta = \delta_c$ .

### 1.3.1. Fermi surface collapse and break-down of Kondo effect

Microscopically, heavy-fermion systems can be modeled as a lattice of localized  $f$  electron moments that are coupled to a band of conduction electrons, the well known Kondo lattice model (Eq.(1.16)). The local moments lose their identity by forming a many body spin singlet with all the conduction electrons, leading to an entangled state. Kondo resonances appear as charge carriers, and  $f$  electrons remember their localized moment origin by possessing a heavy mass. Kondo resonances are part of the electronic excitation spectrum, they must be accounted for in the Fermi surface, leading to a notion of a large Fermi surface. Two types of QCPs arise, depending on the behavior of the Kondo singlet as the system approaches the QCP from paramagnetic side.

When the Kondo singlet is still intact across the antiferromagnetic transition at zero temperature, the only critical degrees of freedom are the fluctuations of the magnetic order parameter. In this case, the antiferromagnetically ordered phase in the immediate proximity to the QCP can be described in terms of a spin-density-wave (SDW) order of the heavy quasiparticles in the paramagnetic phase. The QCP is referred to as the SDW type, which is in the same class as that already considered by Hertz [35, 36, 37]. On the other hand, when the Kondo singlet exists only in the paramagnetic phase, the onset of magnetic order is accompanied by a breakdown of the Kondo effect. The quantum criticality incorporates not only the slow fluctuations of the antiferromagnetic order parameter but also the emergent degrees of freedom associated with the breakup of the Kondo singlet. The corresponding transition is referred to as locally critical [38, 39] and the antiferromagnetic transition is accompanied by a localization of the  $f$  electrons. The distinction of the two types of QCPs can also be made in terms of

energetics. The key quantity to consider is the energy scale  $E^*$ , which dictates the breakup of the entangled Kondo singlet state as the system moves from the heavy Fermi-liquid side toward the quantum critical regime. A reduction of the  $E^*$  scale upon approaching the magnetic side is to be expected because the development of antiferromagnetic correlations among the local moments reduces the strength of the Kondo singlet [40, 41]. When  $E^*$  remains finite at the antiferromagnetic QCP, the Kondo singlet is still formed, and the quantum criticality falls in the universality class of the SDW type (Fig. 1.2, panel b). When the  $E^*$  scale continuously goes to zero at the antiferromagnetic QCP, a critical Kondo breakdown accompanies the magnetic transition (Fig. 1.2, panel a). The consequences of the Kondo breakdown for the change of the Fermi surface is illustrated in Fig. 1.2. When  $E^*$  is finite, the Kondo singlet ground state supports Kondo resonances, and the Fermi surface is large and contains both conduction and localized electrons (Fig. 1.2, panel d). When the  $E^*$  scale becomes zero, the ground state is no longer a Kondo singlet, and there are no fully developed Kondo resonances. Correspondingly, the Fermi surface is small (Fig. 1.2, panel c), incorporating only the conduction electrons. Examples for SDW quantum criticality are CePd<sub>2</sub>Si<sub>2</sub> [42], CeCu<sub>2</sub>Si<sub>2</sub> [43], CeNi<sub>2</sub>Ge<sub>2</sub> [44]. The breakdown of the Kondo effect has been also realized in some heavy-fermion compounds, a famous example being YbRh<sub>2</sub>Si<sub>2</sub> where the Hall coefficient changes abruptly across the magnetic transition, signaling the Fermi surface reconstruction [14].

Direct measurements of Fermi surface are typically done by using angle-resolved photoemission spectroscopy (ARPES). In spite of impressive recent developments, ARPES still does not have the resolution to study heavy-fermion metals in the required sub-Kelvin temperature range. The other well established tool to probe Fermi surfaces is the de Haas-van Alphen (dHvA) technique, which, however, requires a large magnetic field of several teslas.

### 1.3.2. Non-Fermi liquid behavior

One of the interesting phenomena which happens around a QCP is the non-Fermi liquid behavior. In Fermi liquids the excitations have a one-to-one correspondence to those of a noninteracting Fermi gas with the well-known behavior of the specific heat  $C = \gamma T$  with  $\gamma$  independent of temperature  $T$  in the limit  $T \rightarrow 0$ , a Pauli susceptibility  $\chi$  independent of  $T$ , and a  $T$ -dependent electrical resistivity contribution  $\Delta\rho = AT^2$  arising from electron-electron collisions. In fact, most heavy-fermion systems have been described within the framework of Fermi-liquid theory, albeit with huge effective masses  $m^*$  of the quasiparticles exceeding the free-electron mass by a factor of up to several hundred, and correspondingly to huge values of  $\gamma$ ,  $\chi$ , and  $A$  [45].

Non-Fermi liquid behavior also has been observed for some heavy fermion materials

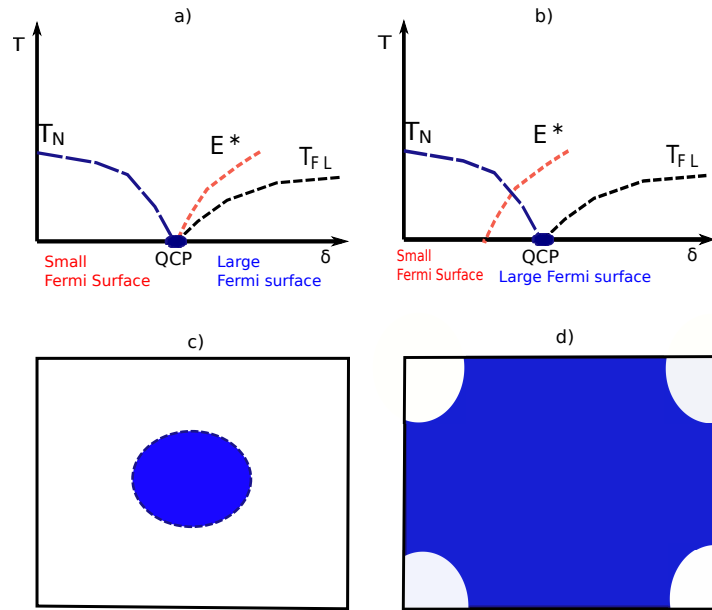


Figure 1.2.: Schematic phase diagrams displaying two classes of quantum critical points. Temperature/energy scales vs. control-parameter  $\delta$  has been shown, (a) illustrating quantum criticality with critical Kondo destruction and (b) of the spin-density-wave type.  $T_N$  represents the Neel temperature and  $T_{FL}$  the onset of the low-temperature Fermi liquid regime.  $E^*$  marks an energy scale separating two types of ground states, one with a large Fermi surface (Kondo resonance fully developed, and  $f$  electrons delocalized) and the other with a small Fermi surface (static Kondo screening absent, and  $f$  electrons localized), (c) small Fermi surface, (d) large Fermi surface.

[46]. In the non-Fermi liquid regime the specific heat, Pauli susceptibility, and resistivity have a following behavior with temperature.

$$\begin{aligned} C/T &\sim -\ln\left(\frac{T}{T_0}\right) \\ \chi &\sim T^{-\beta} \\ \Delta\rho &= -T. \end{aligned} \tag{1.17}$$

Two conceptionally very different origins for this strikingly different behavior have been invoked. (a) A two-channel Kondo effect due to the electrical quadrupolar interaction that might be for instance present in Uranium alloys where the  $U$  atoms are in a  $5f$  atomic configuration, and also in  $Ce$  alloys of hexagonal and cubic  $Ce^{3+}$  site symmetry [47, 48]. (b) The proximity of magnetic order and the concomitant onset of long-range correlations might lead to a breakdown of the Fermi-liquid description. This suggestion is based on the observation of a scaling behavior in the magnetic field and temperature dependence of the specific heat  $C$  and the magnetization  $M$  [49].

### 1.3.3. Heavy fermion superconductivity

Heavy-fermion materials like other compounds could become superconductor. The first discovery of superconductivity in heavy-fermion materials dates back to 1976 by Steglich et al. [21] who observed superconductivity in  $CeCu_2Si_2$ . Since that discovery the list of known heavy-fermion superconductors has grown to include more than a dozen and still is growing [50, 51]. The first discovery by Steglich was met with widespread disbelief. All the measurements of the crystal structure of  $CeCu_2Si_2$  pointed to the fact that the  $Ce$  ions were in a  $Ce^{3+}$  or  $4f^1$  configuration. Yet that meant one local moment per unit cell which required an explanation of how these local moments do not destroy superconductivity, but rather, are part of its formation. This was strange at the time because the conventional wisdom was that magnetism and superconductivity are mutually exclusive. Tiny concentration of magnetic impurities is known to produce a lethal suppression of superconductivity in conventional metals. Early work on the interplay of the Kondo effect and superconductivity by Maple et al. [52], did suggest that the Kondo screening suppresses the pair breaking effects of magnetic moments, but the implication of these results was slowly digested. While the pairing mechanism in heavy-fermion superconductivity is not understood yet, alike in high temperature superconductors, the common belief is that pairing is mediated by magnetic fluctuation (the so-called magnetic mediated superconductivity). In a conventional superconductor, the binding of electrons into the paired states that collectively carry the supercurrent is mediated by phonons. In the case of the heavy fermion superconductors, for example, the  $CePd_2Si_2$  and  $CeIn_3$  [53], the charge carriers might

bound in pairs by spin exchange. Indeed the pairing symmetry in the superconducting phase seems to support this view point, in analogy with cuprates, though the question is still controversial [34]. In fact heavy electron superconductors are mainly anisotropic superconductors, in which the gap function vanishes at points, or more typically along lines on the Fermi surface [54, 55, 56]. The nodal  $d$ -wave character of superconducting pairing in one of the famous  $Ce$  based heavy-fermion compounds  $CeCoIn_5$  has been confirmed in a very recent experimental work [57] based on the high-resolution scanning tunneling microscopy (STM) technique.

Interplay of magnetism and superconductivity in heavy-fermion materials is another issue. This interplay has shown considerable variety by showing competition or coexistence of magnetic and superconducting order parameters. One of the main characteristic of the heavy-fermion superconductors is the emergence of superconductivity around the quantum critical point. Appearance of superconductivity in the vicinity of magnetism reminds pairing correlations in the cuprates. The phase diagram for  $CePd_2Si_2$  [42] (see Fig. 1.3) is reminiscent of theoretical discussions of unconventional superconductivity near an SDW instability. Inelastic neutron scattering studies have identified fluctuations close to the incommensurate ordering wave vector of the nearby SDW and have shown that such fluctuations play a dominant role in driving superconducting pairing [43], confirming earlier theoretical predictions.

Some heavy fermions also show the coexistence of antiferromagnetism with superconductivity in the neighborhood of superconducting phase. The typical example is  $CeRhIn_5$  with the pressure-temperature phase diagram like the one illustrated in Fig. 1.4. Generally, one of the common features of the heavy fermion superconductors is the large values of the electronic specific heat coefficient ( $C/T$ ) at  $T_c$ , order of a few hundreds to even thousands  $mJ/mol - K^2$ , indicating that the heavy quasiparticles participate in the superconducting pairing. Fig. 1.5 shows the temperature variation of the specific heat  $C$  divided by the temperature for four heavy fermion superconductors:  $CeCu_2Si_2$ ,  $UBe_{13}$ ,  $UPt_3$  and  $URu_2Si_2$ . By comparison to the BCS behavior for  $s$ -wave superconductors with a full gap opening in all directions of the wavevectors,  $C/T$  does not present an exponential decrease (as described by the  $s$ -wave BCS curve) but a power law dependence with  $T^\alpha$  which is directly related to the presence of line nodes or point nodes in these anisotropic superconductors [58]. Another indication of the non  $s$ -wave pairing of these systems is in their sensitivity to the non-magnetic impurities in contrast to the conventional superconductors where dilute concentrations of non-magnetic impurities have little effect on the superconducting parameters. Indeed non-magnetic impurities like  $Y$ ,  $La$  and  $Th$  strongly suppress superconductivity in these systems, which it has been interpreted as evidence for non  $s$ -wave pairing.

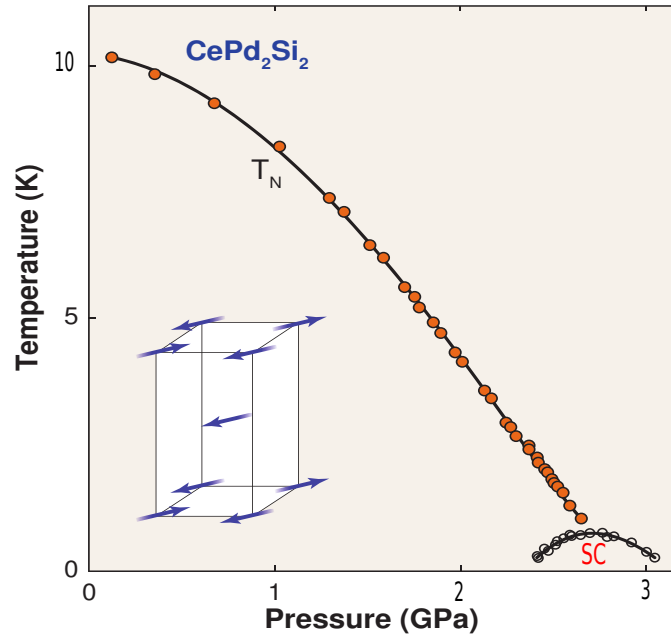


Figure 1.3.: Suppression of antiferromagnetic order through pressure in  $\text{CePd}_2\text{Si}_2$ .  $T_N$  is the Néel transition temperature, and the corresponding antiferromagnetic order is illustrated in the inset. At the boundary of the antiferromagnetism, a phase of unconventional superconductivity arises which covers the quantum critical point.

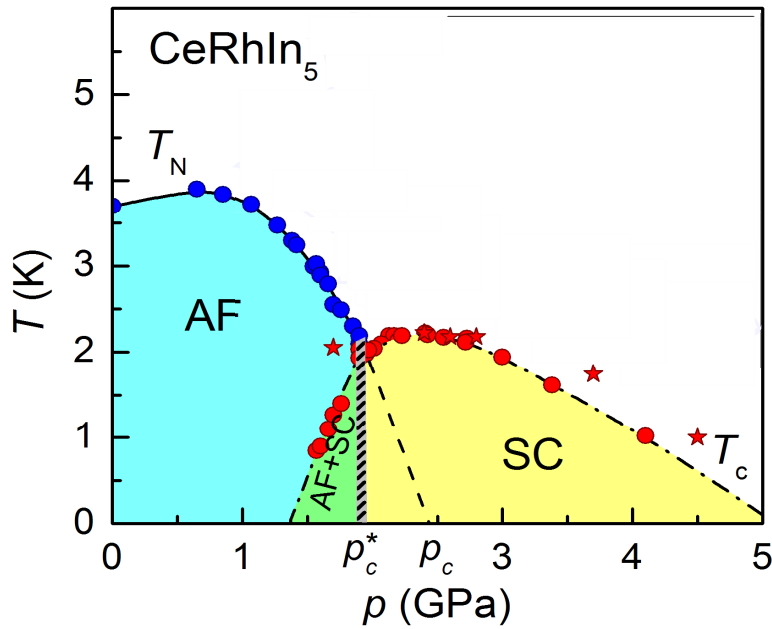


Figure 1.4.: Pressure-Temperature phase diagram of  $\text{CeRhIn}_5$ .

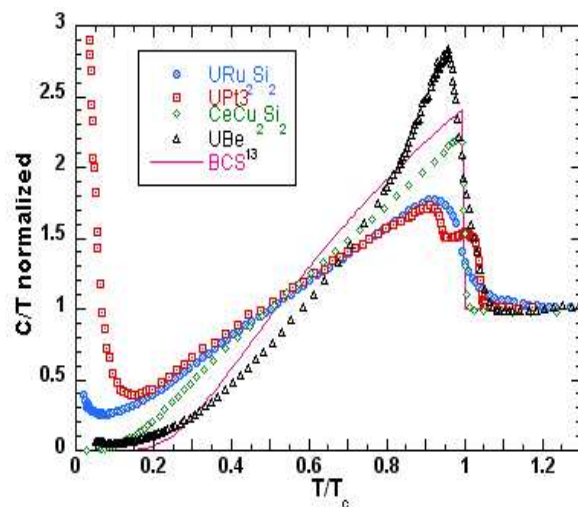


Figure 1.5.: Temperature variation of the specific heat  $C$  divided by the temperature for four heavy fermion superconductors, notice the power law dependence of  $C/T$  for heavy fermion superconductors against exponential decrease in the  $s$ -wave BCS case.

## 2. Methods

### 2.1. Hartree-Fock mean-field

In this section, we briefly describe the simplest strategy to attack an interacting many-body problem. This approach falls under the broad rubric of mean-field theory and is also known as Hartree-Fock theory. The idea behind this technique is to define a non-interacting wave function, which is optimized in order to obtain the best possible ansatz for the exact ground state. Within the Hartree-Fock approximation, the effects of the particle-particle interaction are simulated by an effective external field acting on the particles that is self-consistently generated by the same particles. In order to implement this approach, it is particularly useful to work within the second quantization framework, where a generic interacting Hamiltonian is written as:

$$H = \sum_{\alpha,\beta} t_{\alpha\beta} c_{\alpha}^{\dagger} c_{\beta} + \frac{1}{2} \sum_{\alpha,\beta,\gamma,\delta} U_{\alpha\beta\gamma\delta} c_{\alpha}^{\dagger} c_{\beta}^{\dagger} c_{\gamma} c_{\delta}, \quad (2.1)$$

here  $\alpha$ ,  $\beta$ ,  $\gamma$ , and  $\delta$  include both orbital and spin indices. The case of fermions is considered here.

A particularly enlightening approach to define the Hartree-Fock state  $|\Phi_{HF}\rangle$  relies on the definition of a suitable non-interacting Hamiltonian that depends upon a set of variational parameters  $h_{\alpha\beta}$ :

$$H_{HF} = \sum_{\alpha,\beta} h_{\alpha\beta} c_{\alpha}^{\dagger} c_{\beta}, \quad (2.2)$$

whose ground state is indeed  $|\Phi_{HF}\rangle$ :

$$H_{HF}|\Phi_{HF}\rangle = E_{HF}|\Phi_{HF}\rangle. \quad (2.3)$$

The question is then to determine the variational parameters  $h_{\alpha\beta}$  such that the average value of the actual Hamiltonian in Eq. (2.1) within the subspace of Slater determinants is minimum for the ground state  $|\Phi_{HF}\rangle$  of (2.2). In other words, we should impose that, upon defining

$$E = \langle \Phi_{HF} | H | \Phi_{HF} \rangle, \quad (2.4)$$

then

$$\frac{\partial E}{\partial h_{\alpha\beta}} = 0, \quad (2.5)$$

with  $\partial^2 E / \partial h_{\alpha\beta} \partial h_{\gamma\delta}$  being a positive definite quadratic form.

In order to find the equations that define the variational parameters  $h_{\alpha\beta}$ , let us define:

$$\Delta_{\alpha\beta} = \langle \Phi_{HF} | c_{\alpha}^{\dagger} c_{\beta} | \Phi_{HF} \rangle. \quad (2.6)$$

Then:

$$E_{HF} = \langle \Phi_{HF} | H_{HF} | \Phi_{HF} \rangle = \sum_{\alpha,\beta} h_{\alpha\beta} \Delta_{\alpha\beta}, \quad (2.7)$$

while, the expectation value  $E$  of the interacting Hamiltonian  $H$  is given by:

$$E = \sum_{\alpha,\beta} t_{\alpha\beta} \Delta_{\alpha\beta} + \frac{1}{2} \sum_{\alpha,\beta,\gamma,\delta} \Delta_{\alpha\beta} \Delta_{\gamma\delta} (U_{\alpha\gamma\delta\beta} - U_{\alpha\gamma\beta\delta}), \quad (2.8)$$

which is a functional of the variational parameters  $h_{\alpha\beta}$  (through  $\Delta_{\alpha\beta}$ ). We note that, by the Hellmann-Feynman theorem,

$$\frac{\partial E_{HF}}{\partial h_{\alpha\beta}} = \langle \Phi_{HF} | \frac{\partial H_{HF}}{\partial h_{\alpha\beta}} | \Phi_{HF} \rangle = \Delta_{\alpha\beta}. \quad (2.9)$$

On the other hand, if we differentiate directly Eq. (2.7),

$$\frac{\partial E_{HF}}{\partial h_{\alpha\beta}} = \Delta_{\alpha\beta} + \sum_{\gamma\delta} h_{\gamma\delta} \frac{\partial \Delta_{\gamma\delta}}{\partial h_{\alpha\beta}}. \quad (2.10)$$

Comparing (2.9) with (2.10) we conclude that

$$\sum_{\gamma\delta} h_{\gamma\delta} \frac{\partial \Delta_{\gamma\delta}}{\partial h_{\alpha\beta}} = 0. \quad (2.11)$$

We next note that Eq. (2.5) with  $E$  in Eq. (2.8) is simply

$$\frac{\partial E}{\partial h_{\alpha\beta}} = \sum_{\gamma\delta} \frac{\partial \Delta_{\gamma\delta}}{\partial h_{\alpha\beta}} \left[ t_{\gamma\delta} + \sum_{\mu\nu} \Delta_{\mu\nu} (U_{\gamma\mu\nu\delta} - U_{\gamma\mu\delta\nu}) \right] = 0. \quad (2.12)$$

Therefore, comparing (2.11) with (2.12), we get to the final result that

$$h_{\alpha\beta} = t_{\alpha\beta} + \sum_{\gamma\delta} \Delta_{\gamma\delta} (U_{\alpha\gamma\delta\beta} - U_{\alpha\gamma\beta\delta}). \quad (2.13)$$

These equations can be also interpreted as the definition of  $h_{\alpha\beta}$  in terms of new variational parameters  $\Delta_{\alpha\beta}$ , which must be determined by imposing Eq. (2.6). In this

way, the Hartree-Fock Hamiltonian can be written as:

$$H_{HF} = \sum_{\alpha,\beta} c_{\alpha}^{\dagger} c_{\beta} \left[ t_{\alpha\beta} + \sum_{\gamma,\delta} \Delta_{\gamma\delta} (U_{\alpha\gamma\delta\beta} - U_{\alpha\gamma\beta\delta}) \right]. \quad (2.14)$$

The variational energy of the Hartree-Fock state is given by:

$$E = \langle \Phi_{HF} | H | \Phi_{HF} \rangle = \langle \Phi_{HF} | H_{HF} | \Phi_{HF} \rangle - \frac{1}{2} \sum_{\alpha,\beta,\gamma,\delta} \Delta_{\alpha\beta} \Delta_{\gamma\delta} (U_{\alpha\gamma\delta\beta} - U_{\alpha\gamma\beta\delta}). \quad (2.15)$$

In practice, given an initial ansatz for  $\Delta_{\alpha\beta}$ , the Hamiltonian (2.14) is diagonalized (analytically or numerically):

$$H = \sum_i \omega_j \gamma_j^{\dagger} \gamma_j, \quad (2.16)$$

where the new operators  $\gamma_j$  are related to the  $c_{\alpha}$  by a unitary transformation.

The Hartree-Fock wave function is then obtained by filling the lowest-energy levels  $\omega_j$ :

$$|\Phi_{HF}\rangle = \prod_{j \leq j^*} \gamma_j^{\dagger} |0\rangle, \quad (2.17)$$

where  $j^*$  is the number of electrons in the system. Then, any expectation value like  $\langle \Phi_{HF} | c_{\alpha}^{\dagger} c_{\beta} | \Phi_{HF} \rangle$  can be easily calculated, providing new parameters  $\Delta_{\alpha\beta}$ . The latter ones are used to define a new Hartree-Fock Hamiltonian; the procedure is iterated until convergence.

## 2.2. The variational Monte Carlo

In this section, we describe in some detail the variational Monte Carlo method, which allow us to go beyond the simple mean-field approach by including relevant quantum correlations. In general, for any lattice model, the expectation values over a given variational wave function may be written as a sum over a complete basis set of the Hilbert space. The limitation in performing this sum is that the Hilbert space grows exponentially with the size of the system and, therefore, an exact computation is possible only for few particles/sites. The Monte Carlo method enables us to efficiently evaluate integrals over a multidimensional space by a stochastic sampling. The advantage of this approach is that variational wave functions may also contain correlation terms, that cannot be treated by analytical approaches.

The first step in the variational Monte Carlo method is the definition of a basis of states  $|x\rangle$ . Hereafter, we define an electron configuration  $|x\rangle$  as a state where all the electron positions and  $z$ -components of the spins are defined. In the Kondo lattice

model, a particular configuration is given by:

$$|x\rangle = |\uparrow, \uparrow\downarrow, 0, 0, \downarrow, \dots : \uparrow\uparrow, \downarrow\downarrow, \downarrow\downarrow, \uparrow\uparrow, \downarrow\downarrow, \dots\rangle = c_{1\uparrow}^\dagger c_{2\uparrow}^\dagger c_{2\downarrow}^\dagger c_{5\downarrow}^\dagger \dots f_{1\uparrow}^\dagger f_{2\downarrow}^\dagger f_{3\downarrow}^\dagger f_{4\uparrow}^\dagger f_{5\downarrow}^\dagger \dots |0\rangle. \quad (2.18)$$

The configuration  $|x\rangle$  has two parts. The first one refers to conduction electrons and it allows each site to be occupied by no particle (0), one particle ( $\uparrow$  or  $\downarrow$ ) or two ( $\uparrow\downarrow$ ). The second part refers to localized  $f$  electrons which by constraint singly occupy each site ( $\uparrow\uparrow$  or  $\downarrow\downarrow$ ).

Then, the core of the method is the Metropolis algorithm [59], which generates a Markov chain, i.e., a random walk in configuration space:

$$|x_1\rangle \rightarrow |x_2\rangle \rightarrow |x_3\rangle \rightarrow \dots \quad (2.19)$$

After a certain number of steps required to reach a steady state, configurations are distributed according to a given stationary probability distribution  $p(x)$ . The variational Monte Carlo method consists in the direct application of the Metropolis algorithm to sample the probability distribution given by the modulus squared of a given trial wave function. Since there is a huge literature on the topic, in the following we just briefly describe the method that we have used; in particular, we describe in detail the Stochastic Reconfiguration algorithm [60], which allows us to minimize the variational energy when the trial state depends upon a large number of variational parameters.

The *variational principle* is one of the main pillars of quantum mechanics and tells us that the expectation value of the Hamiltonian  $H$  over *any* trial wave function  $|\Psi\rangle$  is always larger than (or at most equal to) the exact ground state energy  $E_0$ :

$$E = \frac{\langle \Psi | H | \Psi \rangle}{\langle \Psi | \Psi \rangle} \geq E_0. \quad (2.20)$$

This can be easily verified by inserting the complete set of eigenfunctions  $|\phi_i\rangle$  of  $H$  with energies  $E_i$  as follow:

$$\frac{\langle \Psi | H | \Psi \rangle}{\langle \Psi | \Psi \rangle} = \sum_i E_i \frac{|\langle \phi_i | \Psi \rangle|^2}{\langle \Psi | \Psi \rangle} = E_0 + \sum_i (E_i - E_0) \frac{|\langle \phi_i | \Psi \rangle|^2}{\langle \Psi | \Psi \rangle} \geq E_0. \quad (2.21)$$

The variational principle provides a criteria to decide which is the best possible wave function within a set of possible choices: the best wave function is the one that has the lowest possible energy. The evaluation of the energy in Eq. (2.20) is not always easy to perform, since in many-body systems the size of the Hilbert space grows exponentially with the number of particles and/or sites and a direct calculation becomes prohibitively expensive for relatively small sizes. For example, in the Kondo lattice model of Eq. (3.1) there are 8 states per site, so the size of the Hilbert space for  $L$  sites is  $8^L$ ; this restricts

exact treatments to  $L \lesssim 10$ .

Therefore, an alternative way of proceeding must be devised. We can write the expectation value of the energy in the following way:

$$E = \frac{\langle \Psi | H | \Psi \rangle}{\langle \Psi | \Psi \rangle} = \frac{\sum_{x,x'} \Psi^*(x) H_{x,x'} \Psi(x')}{\sum_x |\Psi(x)|^2}, \quad (2.22)$$

where  $\Psi(x) = \langle x | \Psi \rangle$  and  $H_{x,x'} = \langle x | H | x' \rangle$ . Then, Eq. (2.22) can be written in terms of a probability distribution  $p(x)$ , so to implement a Monte Carlo approach:

$$p(x) = \frac{|\Psi(x)|^2}{\sum_{x'} |\Psi(x')|^2}, \quad (2.23)$$

which is a faithful probability distribution, since  $p(x) \geq 0$  and  $\sum_x p(x) = 1$ . Moreover, we define:

$$e_L(x) = \frac{\langle x | H | \Psi \rangle}{\langle x | \Psi \rangle} = \sum_{x'} H_{x,x'} \frac{\Psi(x')}{\Psi(x)}, \quad (2.24)$$

which is called *local energy*. Then, we have:

$$E = \frac{\langle \Psi | H | \Psi \rangle}{\langle \Psi | \Psi \rangle} = \frac{\sum_x |\Psi(x)|^2 e_L(x)}{\sum_{x'} |\Psi(x')|^2} = \sum_x p(x) e_L(x). \quad (2.25)$$

Here, it is important to emphasize the role of the basis set: first of all,  $|x\rangle$  must be chosen such as to easily compute the overlap  $\Psi(x) = \langle x | \Psi \rangle$  (i.e., with a polynomial computational cost). Moreover, the evaluation of the local energy  $e_L(x)$  for a given configuration  $|x\rangle$  must also require a polynomial cost. For instance, if the basis is local, then the Hamiltonian is very sparse, hence, the number of configurations  $|x'\rangle$  connected to  $|x\rangle$  by  $H$  is  $O(L)$ . The local energy depends crucially on the choice of the wave function  $|\Psi\rangle$ . In particular, if  $|\Psi\rangle$  is the exact ground state of  $H$  with eigenvalue  $E_0$ , the local energy does not depend on  $|x\rangle$ , namely  $e_L(x) = E_0$  for each  $|x\rangle$ . This is the so-called zero variance property.

The simplest method to generate a set of configurations according to the probability distribution  $p(x)$  is the Metropolis algorithm [59]: starting from a configuration  $|x\rangle$ , a new configuration  $|x'\rangle$  is firstly proposed and accepted if a random number  $\eta$ , between 0 and 1, satisfies the condition

$$\eta < \frac{p(x')}{p(x)} = \left| \frac{\Psi(x')}{\Psi(x)} \right|^2, \quad (2.26)$$

otherwise the configuration  $|x'\rangle$  is rejected and the new configuration is kept equal to the old one,  $|x'\rangle = |x\rangle$ . In practice, the trial configuration  $|x'\rangle$  may be chosen from the

scattering processes generated by the Hamiltonian. For example, in the Kondo lattice model of Eq. (3.1), we consider the hoppings for conduction electrons and the onsite spin flips.

The calculation of the ratio in Eq. (2.26) would require, for fermions, the evaluation of two Slater determinants, which scale as  $M^3$  ( $M$  being the total number of particles). The fact that the two configurations are related among each other by the displacement of one particle, allows us to perform a more efficient calculation, which for fermions corresponds to  $O(M^2)$  operations.

The evaluation of the total energy  $E$  can be done by generating a sequence of configurations  $|x_n\rangle$  distributed according to the probability distribution  $P(x)$ . The Monte Carlo estimate of the energy is given by:

$$\bar{E} = \frac{1}{N} \sum_{n=1}^N e_L(x_n). \quad (2.27)$$

The central limit theorem ensures that for a large  $N$ ,  $\bar{E}$  approaches the exact value  $E$ :

$$\lim_{N \rightarrow \infty} \bar{E} = E. \quad (2.28)$$

When a finite number  $N$  of configurations are considered, the statistical error can be estimated by

$$\sigma(\bar{E}) = \sqrt{\frac{1}{N} \left( \frac{1}{N} \sum_{n=1}^N e_L^2(x_n) - \bar{E}^2 \right)}. \quad (2.29)$$

However, whenever there is a correlation between successive measurements  $e_L(x_n)$ , this formula gives a biased estimation (the autocorrelation time must be taken into account). Correlation arises because, in practice, two consecutive configurations differ little (for example, by a single exchange of position or a single spin flip). Instead of evaluating the autocorrelation time, it is much better to treat a set of almost non-correlated configurations. Two strategies are often used for that. First, measurements are done only after several, e.g.,  $O(L)$  Markov steps. Second, a binning technique is used. This technique consists of binning together  $M_{bin}$  configurations into  $N_{bin}$  blocks, so to reduce the correlation between them:

$$e_L^{bin}(m) = \frac{1}{M_{bin}} \sum_{n=(m-1) \times M_{bin} + 1}^{m \times M_{bin}} e_L(x_n) \quad (2.30)$$

Then, we have that:

$$\bar{E} = \frac{1}{N_{bin}} \sum_{m=1}^{N_{bin}} e_L^{bin}(m) \quad (2.31)$$

where  $N_{bin} = N/M_{bin}$  (we assume for simplicity that  $N$  is a multiple of  $M_{bin}$ ). The crucial point is that the values of  $e_L^{bin}(m)$  are less correlated than the original  $e_L(x_n)$ ; for  $M_{bin}$  much larger than the autocorrelation time, they are essentially uncorrelated. Therefore, the statistical error of  $\bar{E}$  can be computed by:

$$\sigma(\bar{E}) = \sqrt{\frac{1}{N_{bin}} \left( \frac{1}{N_{bin}} \sum_{m=1}^{N_{bin}} e_L^2(m) - \bar{E}^2 \right)}. \quad (2.32)$$

By using the variational Monte Carlo, all static correlation functions can be easily computed:

$$\langle O \rangle = \frac{\langle \Psi | \hat{O} | \Psi \rangle}{\langle \Psi | \Psi \rangle} = \frac{\sum_x |\Psi(x)|^2 O_x}{\sum_{x'} |\Psi(x')|^2} \quad (2.33)$$

The local value of the operator is  $O_x$  given by

$$O_x = \sum_{x'} \hat{O}_{x,x'} \frac{\Psi(x')}{\Psi(x)} \quad (2.34)$$

with  $\hat{O}_{x,x'} = \langle x | \hat{O} | x' \rangle$ . Therefore, similarly to what has been discussed for the energy, the expectation value  $\langle O \rangle$  of any operator  $\hat{O}$  reduces to average over the values  $O_x$  along the  $N$  steps of the Markov chain:

$$\bar{O} \simeq \frac{1}{N} \sum_x O_x. \quad (2.35)$$

By increasing the lattice size and the number of variational parameters the calculation of Eq. (2.35) will be computationally expensive. In order to speed-up calculations, it is possible to make use of parallelization techniques which is quite easy and straightforward within Monte Carlo. The idea is to use many independent walkers to have different Markov chains, collecting all results together at the end of the simulation. One important point is that each walker must do a different Markov path, it means they should start by having different seeds for the random number generator. For a large number of walkers, the simulations may not scale linearly with the number of walkers; therefore, one has to find the optimum number of walkers for a specified high performance system.

### 2.3. The minimization algorithm

In general, variational wave functions depend upon a set of parameters  $\alpha = \{\alpha_k\}$ , with  $k = 1, \dots, p$ , which refer to local configurations and should be optimized in order to have the best possible representation of the exact ground state. Following the variational

principle described before, this can be done by minimizing the expectation value of the Hamiltonian over the trial state, as a function of the parameters  $\alpha$ . In the following, we show an efficient algorithm to optimize the variational wave function, namely the so-called Stochastic Reconfiguration algorithm that has been introduced in [61].

First of all, let us denote the generic wave function parametrized by the set of  $p$  variational parameters  $\{\alpha\}$  by  $|\Psi(\alpha)\rangle$ . Let  $|\Psi(\alpha^0)\rangle$  be the initial wave function depending on the initial set of parameters  $\alpha^0$ . We now consider a small variation of the parameters  $\alpha_k = \alpha_k^0 + \delta\alpha_k$ . Within the linear approximation the new wave function can be written as:

$$|\Psi(\alpha)\rangle = |\Psi(\alpha^0)\rangle + \sum_{k=1}^p \delta\alpha_k \frac{\partial}{\partial\alpha_k} |\Psi(\alpha^0)\rangle + \mathcal{O}(\delta\alpha_k^2). \quad (2.36)$$

Formally, we can define an operator  $\hat{\mathcal{O}}_k$  such that

$$\hat{\mathcal{O}}_k |\Psi(\alpha)\rangle = \frac{\partial}{\partial\alpha_k} |\Psi(\alpha)\rangle. \quad (2.37)$$

Then, we can write  $|\Psi(\alpha)\rangle$  as

$$|\Psi(\alpha)\rangle = \sum_{k=0}^p \delta\alpha_k \hat{\mathcal{O}}_k |\Psi(\alpha^0)\rangle + \mathcal{O}(\delta\alpha_k^2), \quad (2.38)$$

where we have considered  $\hat{\mathcal{O}}_0 = 1$  and  $\delta\alpha_0 = 1$ . In general, due to normalization of  $|\Psi(\alpha)\rangle$ ,  $\delta\alpha_0 \neq 1$  and one can redefine

$$\delta\alpha_k \rightarrow \delta\alpha_k / \delta\alpha_0. \quad (2.39)$$

Eq. (2.38) can be interpreted as the expansion of  $|\Psi(\alpha)\rangle$  on the subspace spanned by  $\{|\Psi(\alpha^0)\rangle, \mathcal{O}_k |\Psi(\alpha^0)\rangle\}$  with  $k = 1, \dots, p$ . In order to find  $|\Psi(\alpha)\rangle$  that improves the variational energy with respect to  $|\Psi(\alpha^0)\rangle$ , one possibility resides in projection methods. A standard procedure of projection methods corresponds to filter out the exact ground state by iteratively applying the Hamiltonian operator to a given trial state. Therefore, we can apply one step of the power method to the starting wave function:

$$|\Psi'\rangle = (\Lambda - H)\Psi(\alpha^0), \quad (2.40)$$

where  $\Lambda$  is a large positive constant such to lower the energy. In general,  $|\Psi'\rangle$  will not have the desired functional form described by  $|\Psi(\alpha)\rangle$ . Therefore, it is not possible to find a set of parameters  $\alpha$  that describe  $|\Psi'\rangle$ . Instead, we can impose that  $|\Psi'\rangle$  coincides with  $|\Psi(\alpha)\rangle$  within the subspace spanned by the  $\mathcal{O}_k |\Psi(\alpha^0)\rangle$  with  $k = 1, \dots, p$ .

By projecting Eqs. (2.38) and (2.40) on the  $k^{\text{th}}$  component of that subspace, we obtain:

$$\langle \Psi(\alpha^0) | \hat{\mathcal{O}}_k (\Lambda - H) | \Psi(\alpha^0) \rangle = \sum_{k'=0}^p \delta\alpha_{k'} \langle \Psi(\alpha^0) | \hat{\mathcal{O}}_k \hat{\mathcal{O}}_{k'} | \Psi(\alpha^0) \rangle, \quad (2.41)$$

which define a system of  $(p+1)$  linear equations that can be solved to calculate the parameters  $\delta\alpha_k$ .

These equations can be slightly simplified by decoupling the  $k=0$  term from the other ones:

$$\delta\alpha_0 = \Lambda - E - \sum_{k=1}^p \delta\alpha_k \langle \hat{\mathcal{O}}_k \rangle, \quad (2.42)$$

where  $\langle \dots \rangle$  indicates the average over  $|\Psi(\alpha^0)\rangle$ . Then, for  $k \neq 0$  we obtain:

$$\langle H \rangle \langle \hat{\mathcal{O}}_k \rangle - \langle H \hat{\mathcal{O}}_k \rangle = \sum_{k'} \left( \langle \hat{\mathcal{O}}_{k'} \hat{\mathcal{O}}_k \rangle - \langle \hat{\mathcal{O}}_{k'} \rangle \langle \hat{\mathcal{O}}_k \rangle \right) \delta\alpha_{k'}. \quad (2.43)$$

In the left-hand side of this equation, we recognize the generalized forces:

$$f^k = -\frac{1}{2} \frac{\partial E}{\partial \alpha_k} = \langle H \rangle \langle \hat{\mathcal{O}}_k \rangle - \langle H \hat{\mathcal{O}}_k \rangle. \quad (2.44)$$

By defining the (positive definite)  $p \times p$  matrix

$$s_{l,k} = \langle \hat{\mathcal{O}}_l \hat{\mathcal{O}}_k \rangle - \langle \hat{\mathcal{O}}_l \rangle \langle \hat{\mathcal{O}}_k \rangle, \quad (2.45)$$

Eq. (2.43) can be written in a compact form:

$$\sum_l \delta\alpha_l s_{l,k} = f^k \quad (2.46)$$

Thus, the change on the variational parameters within the Stochastic Reconfiguration algorithm can be found from the solution of a simple linear problem:

$$\delta\alpha_l = \sum_k f^k s_{k,l}^{-1}. \quad (2.47)$$

When updating the variational parameters, a (small) rescaling factor may be used to control the extension of the optimization steps:

$$\alpha_k \rightarrow \alpha_k + \delta t \delta\alpha_k. \quad (2.48)$$

The positive definiteness of the matrix  $s_{k,l}$  ensures that the algorithm converges. In

fact, the energy variation corresponding to a small change in the parameters is:

$$\Delta E = -\delta t \sum_{k=1}^p \sum_{l=1}^p s_{k,l}^{-1} f^k f^l + \mathcal{O}(\delta t^2) \quad (2.49)$$

which is always negative for small enough  $\delta t$ , unless the minimum condition of  $f^k = 0$  is reached.

At equilibrium,  $f^k = 0$ , which implies the Euler equations for the variational minimum:

$$\frac{\partial E(\alpha)}{\partial \alpha_k} = 0. \quad (2.50)$$

Moreover, from Eq. (2.44), the variational wave function fulfills the same property of an exact eigenstate, namely:

$$\langle H \rangle \langle \hat{\mathcal{O}}_k \rangle = \langle H \hat{\mathcal{O}}_k \rangle \quad (2.51)$$

which suggests a good accuracy of the variational state also with respect to the expectation values of the operators  $\mathcal{O}_k$ .

Let us remark that the Stochastic Reconfiguration method is similar to the steepest descent method. The main difference, which allows us to obtain a more efficient algorithm, is that the Stochastic Reconfiguration method takes also into account the variation of the wave function. Indeed, it is straightforward to show, by using the linear approximation (2.36), that Eq. (2.46) is equivalent to the Euler equation with the addition of a constraint related to the norm of the wave function:

$$\frac{\partial [E(\alpha^0) - \lambda(\langle \Psi(\alpha^0) | \Psi(\alpha) \rangle - 1)]}{\partial \alpha_k^0} = 0 \quad (2.52)$$

where  $\lambda$  is a Lagrange multiplier. The fact that we can change the parameters of a large amount, without changing notably the wave function, allows us to reach the minimum in a stable way with fewer iterations.

In the Stochastic Reconfiguration algorithm, the variational  $\delta \alpha_k$  are related not only to the forces, but also to the inverse covariance matrix  $s_{l,k}^{-1}$ , see Eq. (2.46). The diagonal elements of the covariance matrix give direct information about the fluctuations of the operators  $\hat{\mathcal{O}}_k$ . The fact that each component of the force is multiplied by the inverse of the fluctuations allows us to move mainly along the directions where the variance of the corresponding operator  $\hat{\mathcal{O}}_k$  is small. This avoids undesired instabilities due to the fluctuations of the stochastic system. Moreover, the presence of non-zero off-diagonal elements  $s_{l,k}$  allows to move each parameter by taking into account all the other directions at the same time.

In summary, the steps for optimization are as follow:

1. Given a wave function  $|\Psi(\alpha)\rangle$ , we perform a variational Monte Carlo calculation

in order to compute the forces  $f^k$ , as well as the matrix  $s_{l,k}$ .

2. With  $f^k$  and  $s_{l,k}$  at hand, the change  $\delta\alpha_k$  is computed and the parameters are updated as  $\alpha_k \rightarrow \alpha_k + \delta t \delta\alpha_k$ .

3. We check the convergence. Indeed, the stochastic nature of the algorithm implies that the forces  $f^k$  are always determined with some statistical noise. Even when the variational minimum is reached, the parameters will fluctuate around their mean values.

4. Once convergence is reached, we average over a certain number of iterations in order to find the optimal parameters.



## 3. Kondo Lattice Model on 2D Lattice

In this chapter, we investigate the Kondo lattice model on the two-dimensional square lattice at zero temperature. We use the Hartree-Fock approximation and the variational Monte Carlo (VMC) technique to study the ground-state phase diagram. The main aim of our study is looking for the existence of superconducting correlations in the ground state. Moreover, we will also address the evolution of the Fermi surface across the magnetic transition, a topic that has been recently debated. In the following, first we introduce the Kondo lattice model, then we will apply the Hartree-Fock approximation and VMC method to depict the ground state phase diagram; finally, we close the chapter by comparing the mean-field and VMC results and their agreement with the experimental phase diagram of heavy-fermion materials.

### 3.1. Kondo lattice model

Following the discovery of the so-called heavy electron materials, Doniach [5] suggested that these systems could be described by a Kondo lattice model (KLM) [62]:

$$H = -t \sum_{\langle i,j \rangle, \sigma} c_{i,\sigma}^\dagger c_{j,\sigma} + h.c. + J \sum_i S_i \cdot s_i \quad (3.1)$$

where  $\langle i, j \rangle$  denotes nearest-neighbor sites  $i$  and  $j$  and  $c_{i,\sigma}^\dagger$  ( $c_{i,\sigma}$ ) creates (destroys) an itinerant electron at site  $i$  with spin  $\sigma$ ;  $s_i = (s_i^x, s_i^y, s_i^z)$  is the spin operator for the  $c$  electrons, i.e.,  $s_i^\alpha = 1/2 \sum_{\sigma,\sigma'} c_{i,\sigma}^\dagger \tau_{\sigma,\sigma'}^\alpha c_{i,\sigma'}$ ,  $\tau^\alpha$  being the Pauli matrices. Similarly,  $S_i = (S_i^x, S_i^y, S_i^z)$  is the spin operator for the localized  $f$  electrons,  $S_i^\alpha = 1/2 \sum_{\sigma,\sigma'} f_{i,\sigma}^\dagger \tau_{\sigma,\sigma'}^\alpha f_{i,\sigma'}$ . By constraint there is one  $f$  electron per site and the exchange coupling is antiferromagnetic, i.e.,  $J > 0$ . There are two explicit processes in this Hamiltonian (see Fig. 3.1): one is the hopping for conduction electrons and the other is the on-site exchange interaction  $J$  between localized  $f$  and conduction electrons. The Kondo exchange is responsible for the local moment screening (the so called Kondo screening), in which the spin of  $f$  electrons is screened by conduction electrons. The Kondo screening is responsible for the formation of non-magnetic state which happens in large  $J$  limit. In addition, there is an indirect process, which is very important for the ground-state properties. This is the RKKY interaction between local spins that Ruderman, Kittel, Kasuya, and Yosida [63] originally derived by second order perturbation

theory to describe the problem of nuclear spin ordering in a metal

$$H_{RKKY} = -\frac{9\pi}{8} n_c \frac{J^2}{\epsilon_f} \sum_{i,j} \frac{S_i \cdot S_j}{r_{ij}^3} (2k_f \cos(2k_f r_{ij}) - \frac{\sin(2k_f r_{ij})}{r_{ij}}), \quad (3.2)$$

where  $n_c$  is the conduction electron density and  $k_f$  ( $\epsilon_f$ ) is the Fermi wave vector (energy). The RKKY interaction is long range and changes its sign depending on the distance between the pair of  $f$  spins. This oscillatory behavior is generated by the Friedel oscillations of the conduction electrons [64], and may induce magnetic ordering of the localized spins with a characteristic energy given by  $J^2/\epsilon_f$ . Indeed, in the weak-coupling region, this energy dominates over the Kondo energy scale  $T_K \sim \epsilon_f e^{-\frac{\epsilon_f}{J}}$ . In general, as a result of the competition between the Kondo effect and the RKKY mechanism, a quantum phase transition appears, in which the system changes from magnetic to paramagnetic.

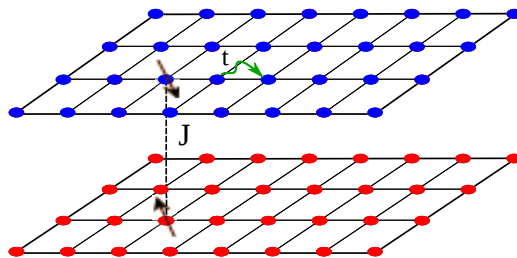


Figure 3.1.: A schematic representation of the Kondo lattice model. There are two species of electrons: the conduction ones, which live in the upper lattice, and the localized ones, which live in the lower lattice. The conduction electrons have a nearest-neighbor hopping with amplitude  $t$ ; conduction and localized electrons interact through the super-exchange coupling  $J$ .

In comparison to the Hubbard model, where the electron correlations come from the on-site Coulomb repulsion between electrons with opposite spin directions, in the KLM the correlations are more subtle, since they derive from the scattering off localized moments.

## 3.2. Hartree-Fock mean field approximation

The simplest approach to the KLM of Eq.(3.1) is the Hartree-Fock approximation, which we introduced in section 2.1. Here, we apply this method to the KLM to derive the ground-state phase diagram. The interaction part of the Hamiltonian (3.1) that contains four fermion operators is the on-site super-exchange term. The Hartree-Fock Hamiltonian is constructed by a mean-field decoupling of the interaction term in all possible channels.

**(i) Magnetic channel**

In this channel we introduce commensurate (staggered) antiferromagnetic order parameters for conduction electrons and localized spins as follow:

$$m_c = -(-1)^i \langle s_i^z \rangle = -\frac{(-1)^i}{2} \langle c_{i\uparrow}^\dagger c_{i\uparrow} - c_{i\downarrow}^\dagger c_{i\downarrow} \rangle \quad (3.3)$$

$$m_f = (-1)^i \langle S_i^z \rangle = \frac{(-1)^i}{2} \langle f_{i\uparrow}^\dagger f_{i\uparrow} - f_{i\downarrow}^\dagger f_{i\downarrow} \rangle \quad (3.4)$$

which have opposite signs because of the antiferromagnetic exchange  $J$ .  $m_c$  is the magnetization of conduction electrons which is felt by local spins and similarly  $m_f$  is the magnetization of the local spins felt by conduction electrons. The nonzero value of these order parameters describes the presence of magnetism. Here, we consider the case in which these order parameters do not depend upon the site of the lattice, which in general may not be the case. We also mention that the ferromagnetic phase is also possible for very low concentration of conduction electrons [10], but in this thesis we are not interested in this extreme regime and we focus on fillings close to the compensated regime  $n_c = 1$ , where the antiferromagnetic ordering is relevant.

**(ii) Kondo hybridization channel**

The other order parameter is hybridization that describes the singlet formation between  $c$  and  $f$  electrons. In presence of a broken translational symmetry, due to the presence of nonzero antiferromagnetic order parameters, one must generally consider two different hybridizations in the two sublattices  $A$  and  $B$ :

$$V_1 = \langle c_{i,\uparrow}^\dagger f_{i,\uparrow} \rangle_{i \in A} = \langle c_{i,\downarrow}^\dagger f_{i,\downarrow} \rangle_{i \in B} \quad (3.5)$$

$$V_2 = \langle c_{i,\uparrow}^\dagger f_{i,\uparrow} \rangle_{i \in B} = \langle c_{i,\downarrow}^\dagger f_{i,\downarrow} \rangle_{i \in A} \quad (3.6)$$

The nonzero value of these order parameters describes the Kondo effect in the system and their magnitude reflects the degree of screening and the contribution of the local spin degrees of freedom in the Fermi volume.

**(iii) Pairing channel**

In general, one could also allow for singlet pairing between  $c$  and  $f$  electrons. At the mean-field level, the only pairing order parameter which comes from the decoupling of the Hamiltonian is the on-site singlet pairing:

$$\Delta_{BCS} = \langle c_{i\uparrow}^\dagger f_{i\downarrow}^\dagger \rangle = \langle c_{i\downarrow}^\dagger f_{i\uparrow}^\dagger \rangle \quad (3.7)$$

However, at the mean-field level, this superconducting order parameter is not independent from the hybridization, because of the charge-isospin  $SU(2)$  symmetry displayed

by the  $f$  electrons. This is clear if one perform the following canonical transformation:

$$f_{i\downarrow}^\dagger \rightarrow f_{i\uparrow} \quad (3.8)$$

$$c_{i\downarrow}^\dagger \rightarrow -c_{i\uparrow} \quad (3.9)$$

which changes the superconducting order parameter into hybridization. The equivalence between hybridization and on-site pairing can be also seen from the fact that the two mean-field parameters lead to the same self-consistency equations. Based on this fact, in the following we do not consider the superconducting order parameter.

By considering magnetic and hybridization order parameters, after Fourier transformation in momentum space, the mean-field approximation of the KLM can be written in a simple  $4 \times 4$  matrix form:

$$\mathcal{H}_{\text{AF}} = \sum_{k \in \text{MBZ}, \sigma} \begin{bmatrix} c_{k,\sigma}^\dagger & c_{k+Q,\sigma}^\dagger & f_{k,\sigma}^\dagger & f_{k+Q,\sigma}^\dagger \end{bmatrix} \times \begin{bmatrix} \epsilon_k & \frac{1}{2}Jm_f\sigma & -\frac{3}{4}JV & -\frac{1}{4}JV'\sigma \\ \frac{1}{2}Jm_f\sigma & -\epsilon_k & -\frac{1}{4}JV'\sigma & -\frac{3}{4}JV \\ -\frac{3}{4}JV & -\frac{1}{4}JV'\sigma & -\mu_f & -\frac{1}{2}Jm_c\sigma \\ -\frac{1}{4}JV'\sigma & -\frac{3}{4}JV & -\frac{1}{2}Jm_c\sigma & -\mu_f \end{bmatrix} \begin{bmatrix} c_{k,\sigma} \\ c_{k+Q,\sigma} \\ f_{k,\sigma} \\ f_{k+Q,\sigma} \end{bmatrix} + \text{const}, \quad (3.10)$$

where the sum over  $k$  is restricted to the reduced (magnetic) Brillouin zone (see Fig. 3.2). The  $c$  electron dispersion is given by:

$$\epsilon_k = -2t[\cos(k_x) + \cos(k_y)]. \quad (3.11)$$

where we set  $t = 1$  as a unit of energy in the following. A Lagrange multiplier  $\mu_f$  has

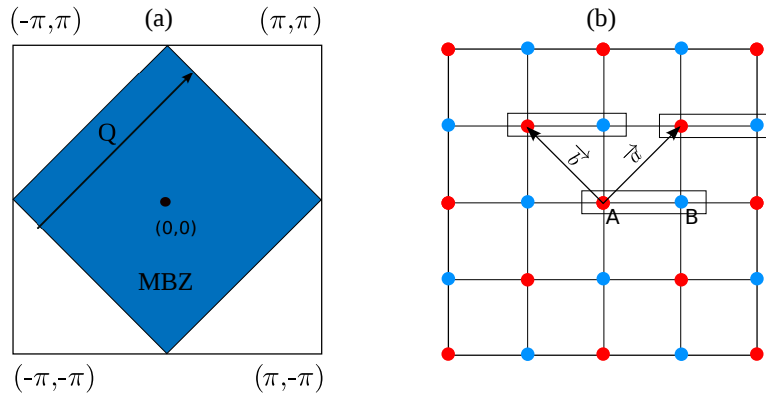


Figure 3.2.: a) Magnetic Brillouin zone, b) Antiferromagnetic unit cell with two sublattices  $A$  and  $B$ .

been included to enforce the constraint of one localized  $f$  electron per site on average:

$$\frac{1}{N} \sum_{i\sigma} \langle f_{i\sigma}^\dagger f_{i\sigma} \rangle = 1 \quad (3.12)$$

$V$  and  $V'$  are uniform and staggered components of the hybridization respectively, which have the following definition:

$$V = \frac{1}{2}(V_1 + V_2) \quad (3.13)$$

$$V' = \frac{1}{2}(V_1 - V_2) \quad (3.14)$$

The constant term is

$$const = Jm_c m_f N + \frac{3}{2} J V^2 N - \frac{1}{2} J V'^2 N \quad (3.15)$$

and should be considered for proper comparison of energies.

The self-consistency conditions of Eqs.(3.3), (3.4), (3.5), and (3.6) are solved numerically on finite size systems with  $N$  sites, a number that must be scaled to get reliable estimates in the thermodynamic limit. We mention that an analytic solution of the problem is possible only in the compensated regime ( $n_c = 1$ ) [65], while in general, numerical calculations are needed. In practice, we numerically diagonalize  $4 \times 4$  matrix for all  $k$  points independently and then fill the bands with the lowest orbitals; the mean-field parameters are numerically calculated and the procedure is iterated until convergence is reached. Depending on the magnitude of mean-field parameters there are three different magnetic states. In the following we shall adopt the notations of Ref.[15]. Whenever the hybridization parameter vanishes, the localized electrons decouple from the conducting ones and do not contribute to the volume enclosed by the Fermi surface; in this case, we have an antiferromagnetic state with a “small” Fermi surface that we denote by AFs. By adding a small hybridization to the AFs, we end up with a state which still has a small electron-like Fermi surface, the so-called AFe. In the case where the hybridization is large and the magnetic order parameter is small, we have a hole-like Fermi surface, the so-called AFh. Here the  $f$  electrons participate to the total volume enclosed by the Fermi surface, which is therefore “large”. Finally, if magnetism disappears, the Fermi surface remains large since hybridization is finite and we end up with paramagnetic normal metal (PM). A qualitative picture of all these states is depicted in Fig. 3.3.

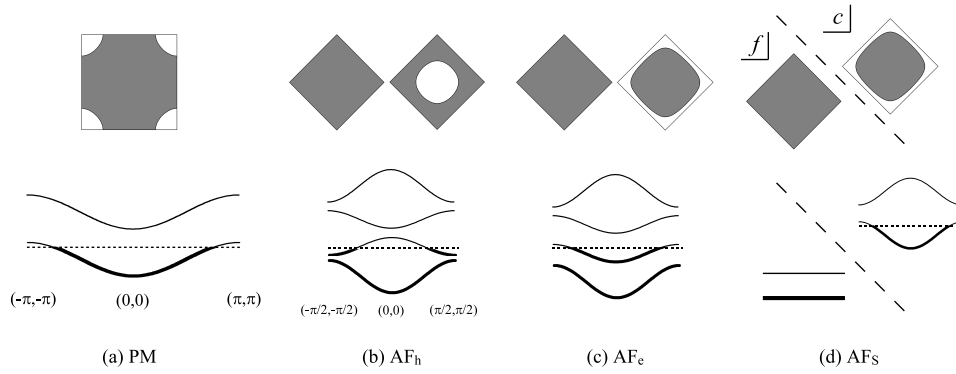


Figure 3.3.: Fermi surfaces and band dispersions of the four different possible states. (a) paramagnetic metal, (b) AF<sub>h</sub>, (c) AF<sub>e</sub> and (d) AF<sub>s</sub>. This figure has been reproduced from Ref. [15].

### 3.2.1. Mean-field results

The mean field phase diagram as a function of  $J$  and the electron density  $n_c$ , is reported in Fig. 3.4. For  $n_c > 0.81$  there are two distinct phase transitions. When  $J$  is small,

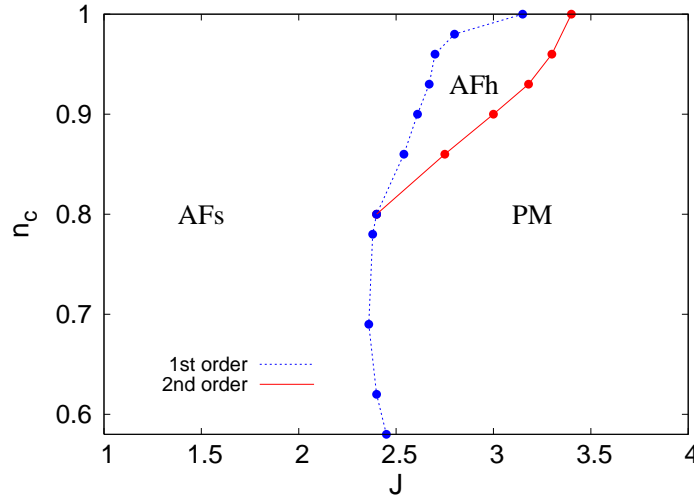


Figure 3.4.: Mean-field ground state phase diagram in the  $J - n_c$  plane.

the ground state has antiferromagnetic long-range order and displays a small Fermi surface, namely it is the AF<sub>s</sub> state. Here, the local  $f$  electrons are totally decoupled from the conducting ones ( $V$  and  $V'$  are zero) and do not contribute to the Fermi surface. This regime is dominated by the RKKY interaction that generates a magnetic pattern in the localized spins, and consequently also in the conducting electrons. The magnetization of  $f$  electrons is saturated, i.e.,  $m_f = 0.5$ , while  $m_c$  is a smooth function, slightly increasing with  $J$ . Within this mean-field decoupling, for  $n_c = 1$  the magnetic

transition takes place at  $J_c = 3.4$ , quite different from the value obtained in Ref.[65], which misses an important Fock term. By increasing  $J$ , the Kondo mechanism becomes competitive with RKKY interaction and we enter into another antiferromagnetic phase, where  $c$  and  $f$  electrons are hybridized. Here, there is a hole-like Fermi surface and, therefore, the phase is AFh. The hybridizations have a finite jump at the transition, which is, therefore first order. We remark that the staggered hybridization  $V'$  remains always quite small, and the Kondo screening is mainly due to  $V$ . In Fig. 3.5 the behavior of the hybridizations and the total magnetization  $m_z = m_f - m_c$  is shown for different conduction electron densities. Eventually, by further increasing the local exchange, the Kondo mechanism prevails and the system becomes a paramagnetic metal where conduction electrons screen the local moments. The transition between the AFh phase and the paramagnetic metal is second order, with the magnetization that goes continuously to zero (see Fig. 3.5, right panel). Moreover, the hybridizations are continuous through the transition and the topology of the Fermi surface does not change.

For smaller values of the conduction electron density, i.e.,  $n_c < 0.81$ , the AFh state cannot be stabilized anymore and there are only two phases: the AFs for small Kondo exchange and the paramagnetic metal for large ones. The phase transition between them is first order. Both the antiferromagnetic order parameter and the hybridization  $V$  change abruptly from zero to a finite value while  $V'$  is always vanishing (see Fig. 3.5, left panel). In this case the breakdown of Kondo effect happens together with the appearance of magnetism and the topology of the Fermi surface changes across the transition.

### 3.3. Variational Monte Carlo approach

One of the flaws of mean-field in treating KLM is in imposing the constraint of one  $f$  electron per site

$$\sum_{\sigma} f_{i\sigma}^{\dagger} f_{i\sigma} = 1 \quad (3.16)$$

on average and not on each site independently. In order to go beyond the mean-field approximation, we consider here correlated variational wave functions, in which the constraint of one  $f$  electron per site is imposed exactly via a Gutzwiller projector. This is achieved through the projected variational wave function:

$$|\Psi\rangle = \mathcal{P}_f |\Psi_0\rangle \quad (3.17)$$

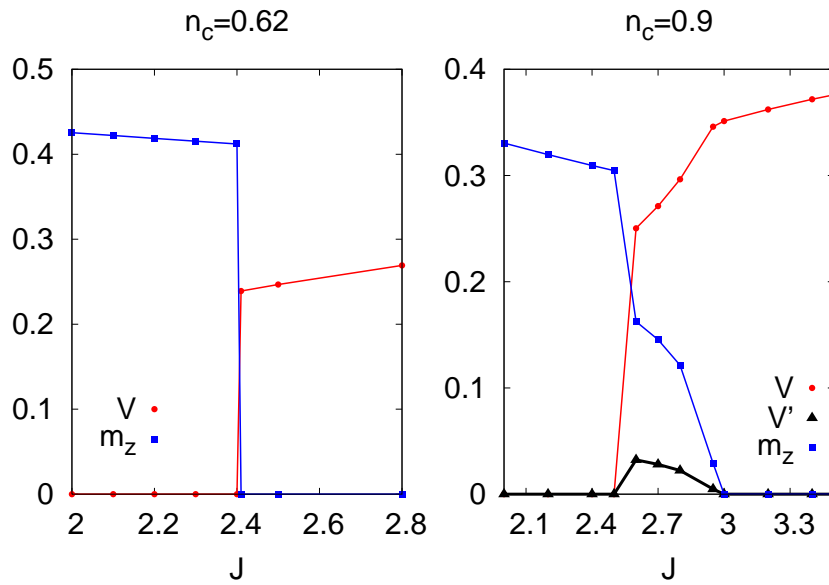


Figure 3.5.: Mean-field order parameters for two conduction electron densities. (Left panel) For  $n_c = 0.62$  there is a discontinuous change for  $V$  and  $m_z$  which signals first order transition. (Right panel) For  $n_c = 0.9$  there are two transitions, discontinuous one which happens between AFs and AFh, and continuous one which connects AFh to PM. Note that in this density  $V'$  is finite in AFh phase but not comparable with  $V$ .

where  $\mathcal{P}_f$  is the projector which enforces single occupation of  $f$  orbitals on each site.

$$\mathcal{P}_f = \prod_i \left[ n_{i\uparrow}^f (1 - n_{i\downarrow}^f) + n_{i\downarrow}^f (1 - n_{i\uparrow}^f) \right] \quad (3.18)$$

Here,  $|\Psi_0\rangle$  is an uncorrelated wave function defined as the ground state of a suitable noninteracting variational Hamiltonian. Since the variational Monte Carlo technique does not suffer from the negative sign problem, like quantum Monte Carlo method [11, 66], it can be easily applied to the case with  $n_c < 1$ . In the following, we describe in detail how the uncorrelated state  $|\Psi_0\rangle$  is constructed for various phases.

### (i) Paramagnetic state

For a paramagnetic state, we construct  $|\Psi_0\rangle$  from the one-body Hamiltonian

$$H_{\text{PM}} = \sum_{k,\sigma} \begin{bmatrix} c_{k,\sigma}^\dagger & f_{k,\sigma}^\dagger \end{bmatrix} \begin{bmatrix} \epsilon_k & V \\ V & \epsilon_k^{ff} - \mu_f \end{bmatrix} \begin{bmatrix} c_{k,\sigma} \\ f_{k,\sigma} \end{bmatrix}, \quad (3.19)$$

where  $V$  is a variational parameter which controls the degree of  $c - f$  hybridization and  $\mu_f$  is a control parameter for  $f$  level occupancy; in addition, we consider also the hopping of the  $f$  electrons ( $\chi_{ff}$ ) as a new variational parameter:

$$\epsilon_k^{ff} = -2\chi_{ff}[\cos(k_x) + \cos(k_y)]. \quad (3.20)$$

We would like to emphasize that due to the presence of the Gutzwiller projector, the one-body Hamiltonian may contain terms that are not allowed at the simple mean-field level, such as the hopping of the  $f$  electrons ( $\chi_{ff}$ ).

### (ii) Superconducting state

In the variational wave function, one could easily include pairing correlations that cannot be present within the mean-field approximation. Specifically, one can add to the Hamiltonian of Eq.(3.19) suitable pairing order parameters. In real space, the possible pairings are as follow:

$$\Delta_{i,j}^{ff} = \langle f_{i,\uparrow}^\dagger f_{j,\downarrow}^\dagger + f_{j,\uparrow}^\dagger f_{i,\downarrow}^\dagger \rangle \quad (3.21)$$

$$\Delta_{i,j}^{cc} = \langle c_{i,\uparrow}^\dagger c_{j,\downarrow}^\dagger + c_{j,\uparrow}^\dagger c_{i,\downarrow}^\dagger \rangle \quad (3.22)$$

$$\Delta_{i,j}^{cf} = \langle c_{i,\uparrow}^\dagger f_{j,\downarrow}^\dagger + f_{j,\uparrow}^\dagger c_{i,\downarrow}^\dagger \rangle \quad (3.23)$$

which can describe both  $s$ -wave or  $d$ -wave configurations depending on the space symmetry.

### (iii) Magnetic state

Antiferromagnetic wave functions are constructed from the following Hamiltonian in

momentum space:

$$H_{\text{AF}} = \sum_{k \in \text{MBZ}, \sigma} \begin{bmatrix} c_{k,\sigma}^\dagger & c_{k+Q,\sigma}^\dagger & f_{k,\sigma}^\dagger & f_{k+Q,\sigma}^\dagger \end{bmatrix} \times \begin{bmatrix} \epsilon_k & m_f \sigma & V & 0 \\ m_f \sigma & -\epsilon_k & 0 & V \\ V & 0 & \epsilon_k^{ff} - \mu_f & -m_c \sigma \\ 0 & V & -m_c \sigma & -\epsilon_k^{ff} - \mu_f \end{bmatrix} \begin{bmatrix} c_{k,\sigma} \\ c_{k+Q,\sigma} \\ f_{k,\sigma} \\ f_{k+Q,\sigma} \end{bmatrix}, \quad (3.24)$$

where  $m_c$  and  $m_f$  are variational parameters for the staggered magnetization of the conduction electrons and local spins, respectively. If we set  $m_c = m_f = 0$ , Eq.(3.24) reduces to Eq.(3.19). We would like to remind again that depending on the magnitude of  $m_c, m_f$  and  $V$  there are three different kind of magnetic states. (a) AF with holelike Fermi surface (AFh), (b) AF with electronlike Fermi surface (AFe) and (c) AF without  $c - f$  hybridization. In AFh and AFe states,  $V$  is finite; i.e., the  $c$  and  $f$  electrons hybridize with each other through the Kondo screening. The state called AFs represents the small Fermi surface which has no Kondo screening ( $V = 0$ ). This phase exists at the mean-field level but not within variational Monte Carlo, as it is more expensive than AFe (see below).

### (iii) Coexistence of antiferromagnetism with superconductivity

The other variational possibility is a wave function in which both antiferromagnetic and superconducting order parameters are present. The motivation for this stems from the experimental observation of this coexistence phase in some heavy fermion materials. So this state could be made simply by adding pairing parameters of Eqs.(3.21), (3.22), and (3.23) to Eq.(3.24). The resulting Hamiltonian is  $8 \times 8$  matrix (in  $k$  space).

The variational parameters of the noninteracting Hamiltonian are determined so as to minimize the total energy. Because of the presence of the Gutzwiller projector  $\mathcal{P}_f$  we have to use a variational Monte Carlo technique [67] to compute the total energy. In practice, we minimize the variational energy for all the previous states as a function of the exchange coupling  $J$  and the electron density  $n_c$ . Calculations have been performed on clusters with 64, 100, 144, and 256 sites. Suitable boundary conditions have been chosen to obtain closed-shell configurations in  $|\Psi_0\rangle$ .

### 3.3.1. Variational Monte Carlo results

First, we consider just the paramagnetic sector which is richer than the one obtained within mean-field approximation, and can shed some light by disentangling Kondo effect from long-range magnetism. The paramagnetic phase diagram of the KLM, allowing for superconductivity, is shown in Fig. 3.6. We find that, although (on-site or extended)  $s$ -wave pairing is never stabilized, a sizable  $d$ -wave pairing is obtained in a wide range of

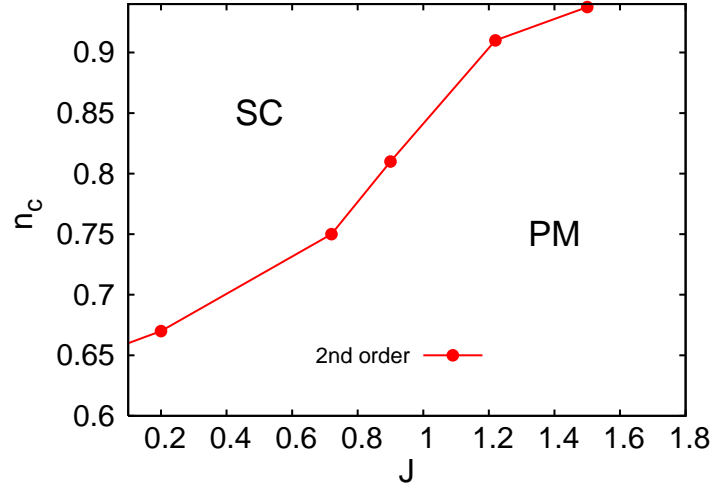


Figure 3.6.: Variational Monte Carlo phase diagram of paramagnetic sector allowing for superconductivity.

parameters, namely for  $J \lesssim 1.5$  and  $n_c \gtrsim 0.65$ , and brings a non-negligible energy gain with respect to a normal phase. The condensation energy (energy difference between superconducting phase and simple metallic phases) is reported in Fig. 3.7 for three values of  $n_c$ . For  $J \lesssim 0.2$ , the pairing correlations of the unprojected state become very small, implying a tiny energy gain with respect to the normal state. We emphasize

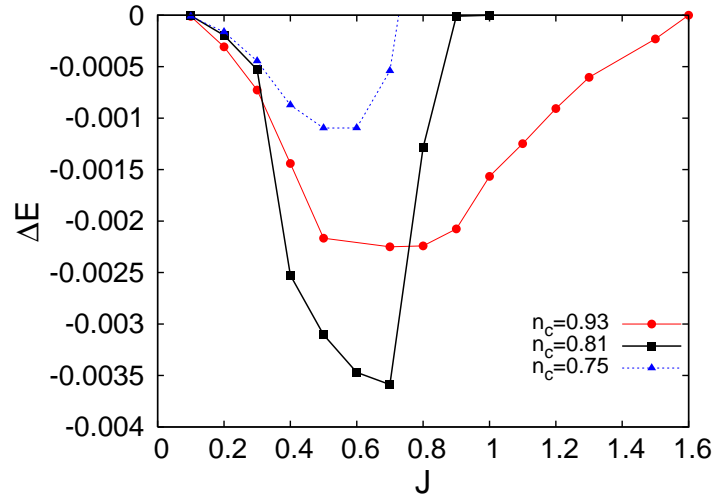


Figure 3.7.: Superconducting condensation energy as a function of  $J$  for three values of  $n_c$ . here and in the following  $\Delta E$  is always energy difference per site.

that superconductivity emerges only thanks to the electronic correlations brought by the Gutzwiller projector  $\mathcal{P}_f$  since pairing does not arise at the mean-field level. A

finite conduction electron  $d$ -wave pairing is thus generated by the antiferromagnetic  $c$ - $f$  exchange, suggestive of similarities to analogous results found in the  $t$ - $J$  model for cuprate superconductors [68, 69]. Indeed, as shown in Fig. 3.7, the condensation energy has a bell like shape, with maximum at some intermediate values of  $J$  and  $n_c$ . The presence of a true superconducting long-range order is also detected by looking to the pair-pair correlation functions:

$$P^2 = \langle \Delta_{i,j}^\dagger \Delta_{l,k} \rangle \quad (3.25)$$

where  $\Delta_{i,j}$  creates a singlet pair of electrons in the neighboring sites  $i, j$  (see Fig. 3.8):

$$\Delta_{i,j}^\dagger = c_{i\uparrow}^\dagger c_{j\downarrow}^\dagger + c_{j\uparrow}^\dagger c_{i\downarrow}^\dagger \quad (3.26)$$

A superconducting order is related to a finite value of  $P^2$  when a large distance between

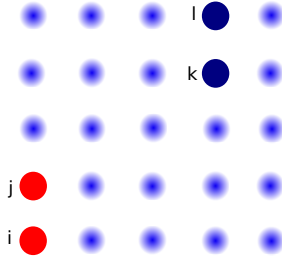


Figure 3.8.: Pairs of sites  $i, j$  and  $l, k$  on the lattice.

the two pairs is considered. To clarify to which extent the presence of  $J$  enhances superconductivity with respect to the non-interacting limit, we calculate the pairing correlations for the superconducting state  $|\Psi\rangle$  and compare them with the ones of free fermions. For the latter ones, the calculation of Eq.(3.25) is straightforward, for detail see Appendix A. Instead, in the presence of the Gutzwiller projection,  $P^2$  must be computed by using variational Monte Carlo.

In Fig. 3.9, we report the pair-pair correlations as a function of the distance (between singlet pairs) for free fermions and the superconducting wave function. For large values of the super-exchange  $J$ , the behavior of correlations remains pretty constant increasing the distance and the value at large distances is sensibly higher than the one of free fermions.

Finally, we would like to mention that a very recent single-site dynamical mean field theory (DMFT) calculation in the paramagnetic sector [70] finds evidence of  $s$ -wave superconductivity, whose maximum strength is reached, for a semicircular density of states, when  $J \sim 1.6$  (translated in our units in which the bandwidth is  $8t$ ) and  $n_c \sim 0.86$ , which we could not reproduce by our simple variational wave function.

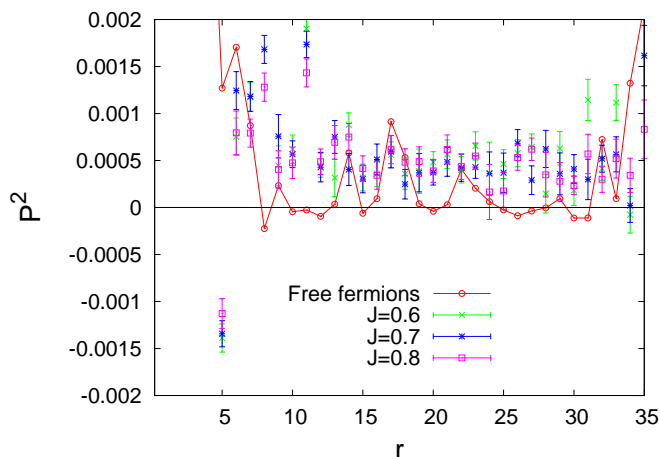


Figure 3.9.: Pair-pair correlation as a function of distance for the superconducting phase. The electron density is  $n_c = 0.86$  and pair-pair correlations for free electrons has been plotted for comparison.

When we leave the paramagnetic sector and allow for antiferromagnetism, the latter prevails over superconductivity, which therefore disappears from the actual phase diagram, see Fig. 3.10. In other words, the energy gain of antiferromagnetism always overcomes that of superconductivity (see Fig. 3.11) ruling out the possibility of a ground state with superconductivity and no magnetic order. This occurs at least in the bipartite nearest-neighbor hopping model that we have considered, where the only source of frustration is the conduction electron density  $n_c$  lower than the compensated regime  $n_c = 1$ .

We observe that the region of stability of the AFe phase is reduced substantially with respect to corresponding AFs found at the mean-field level (we recall that AFe replaces AFs in the more accurate VMC technique), compare Fig. 3.4 with Fig. 3.10, showing that the variational wave function can deal with Kondo screening better than mean field. Thanks to the Gutzwiller projector in VMC there is a substantial energy improvement. In Fig. 3.12 the ground state energy for the PM phase is compared for VMC and simple Hartee-Fock approximation. We see that by increasing  $J$ , the role of the projector is more important and the energy gain is huge.

We also investigated possible coexistence between antiferromagnetism and  $d$ -wave superconductivity, which we indeed found out only in the AFe region. However, we believe this result is only a finite size effect since the energy gain by allowing  $d$ -wave pairing on top of magnetism is tiny (at maximum,  $\Delta E \simeq 10^{-4}t$ ) and, in addition, the size scaling of the actual order parameter (after Gutzwiller projection) suggests a vanishing value in the thermodynamic limit. Indeed, by a direct calculation of the pair-pair correlations of Eq.(3.25) shows that the behavior is similar to the one of free

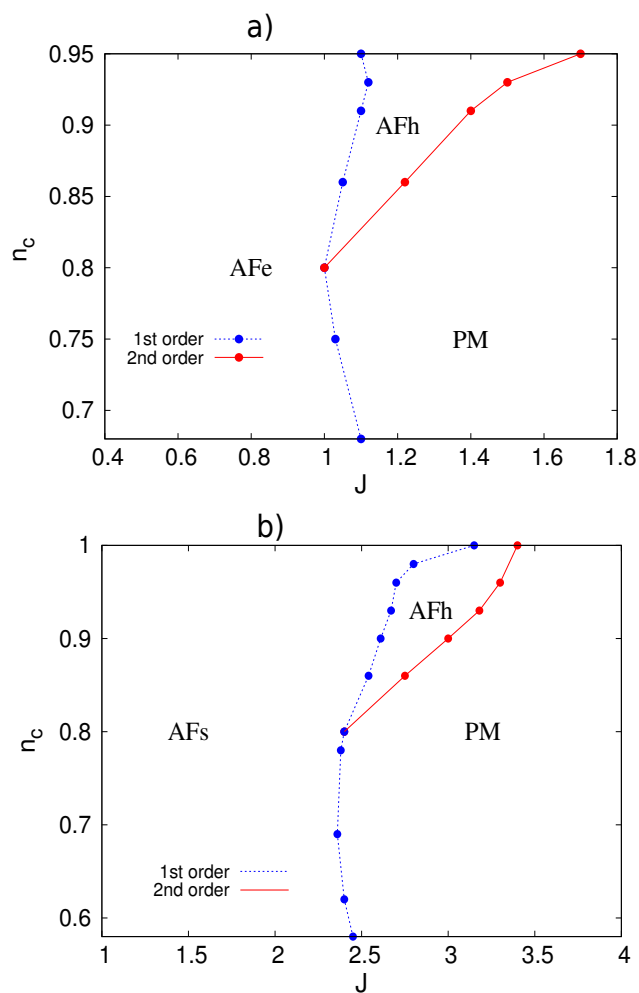


Figure 3.10.: a) Variational phase diagram in the  $J - n_c$  plane. b) Mean Field phase diagram in the  $J - n_c$  plane. Notice that in the VMC phase AFs is replaced by AFe and its region of stability is reduced with respect to the corresponding AFs found at the mean-field level.

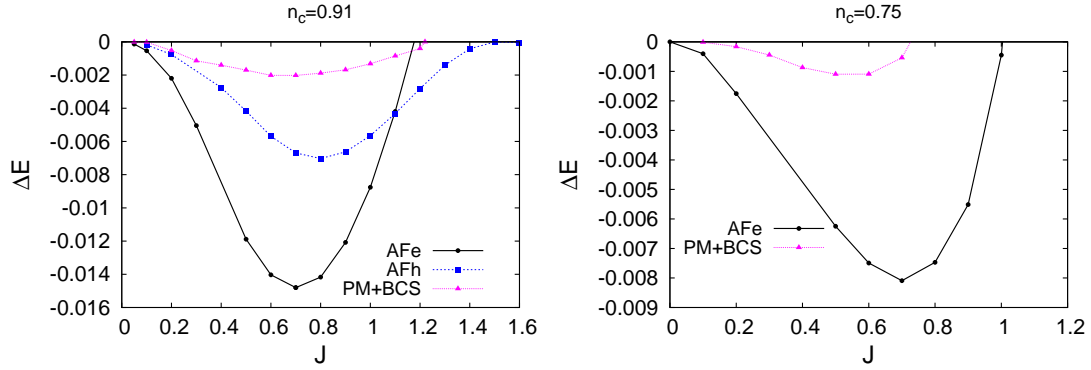


Figure 3.11.: Energy difference of each state compared with the PM state versus exchange coupling  $J$ . (left panel) for  $n_c = 0.91$  (right panel) for  $n_c = 0.75$ . Notice that for  $n_c = 0.75$  there is no stabilized AFh phase. The error bars are on the order of  $10^{-5}$  and are not shown here.

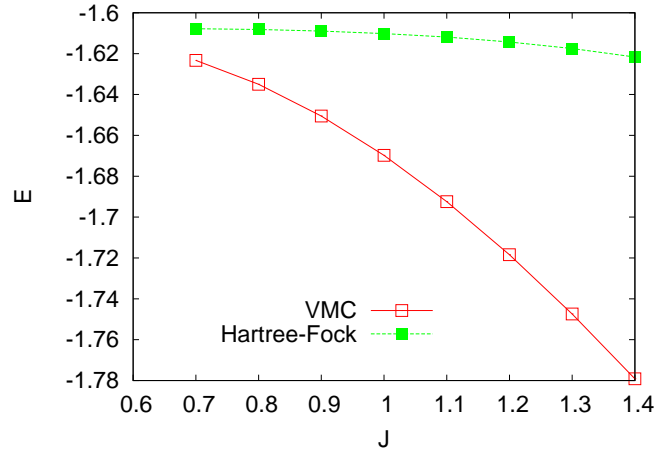


Figure 3.12.: Ground state energy for paramagnetic phase for  $n_c = 0.87$ . Notice the enhancement of energy due to Gutzwiller projector in variational calculation.

fermions, with a practically zero value within errorbars at large distances and large oscillations (see Fig. 3.13).

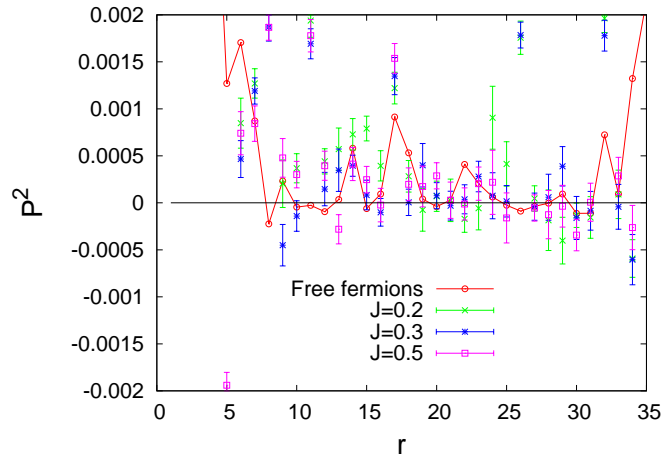


Figure 3.13.: Pair-pair correlation as a function of distance for the best wave function containing both superconductivity and magnetism. The electron density is  $n_c = 0.86$  and pair-pair correlations for free electrons has been plotted for comparison.

### 3.4. Spectral function and Fermi surface topology

In this section we want to consider spectral properties of the KLM. One of the questions which still is alive and under debate is whether the Fermi volume contains the  $f$  electrons or not? Does the breakdown of the Kondo effect happens right of the magnetic transition or not?

Within the Hartree-Fock method we found the *AFs* in which the hybridization is zero and the localized electrons are decoupled from the conduction ones and do not participate in the Fermi volume. Within the variational Monte Carlo, the hybridization parameter  $V$  of the noninteracting auxiliary Hamiltonian is finite throughout the phase diagram. It follows that the zero-temperature variational Fermi surface always includes both  $c$  and  $f$  electrons. However, the optimized  $V$  is tiny in the *AFe* phase and, therefore, a very small temperature can wash away the effects of  $V$  in this phase (but not in the *AFh* and *PM* ones). For this reason we calculate the emission spectrum  $A(k)$  of the auxiliary Hamiltonian at the chemical potential, broadened with a low but finite temperature  $T$ . The  $k$  points where  $A(k)$  is large identify the effective Fermi surface. The spectral function by the definition is:

$$A(k) = - \int d\epsilon A(k, \epsilon) \frac{\partial f(\epsilon)}{\partial \epsilon} \quad (3.27)$$

in which  $f(\epsilon)$  is Fermi distribution, and  $A(k, \epsilon)$  for emission spectrum is as follow:

$$A(k, \epsilon) = \sum_{n>0} |\langle n | c_{k,\sigma} | 0 \rangle|^2 \delta(\epsilon - E_n + E_0) \quad (3.28)$$

where  $|n\rangle$  are the unprojected states of the auxiliary Hamiltonian, with energies  $E_n$ . In Fig. 3.14 we show  $A(k)$  in the paramagnetic sector allowing for superconductivity,  $A(k)$  has been plotted for four different values of  $J$ , two well inside the superconducting region and two across the transition to the normal phase. Since the transition is continuous, the  $T > 0$  Fermi surface continuously change from electron-like to hole-like. A large spectral weight along the zone diagonals in the superconducting phase is observed whenever sizable pairing correlations are present, because of  $d$ -wave symmetry. In Fig. 3.15 we draw  $A(k)$  for different values of  $n_c$  and  $J$  when also magnetism is considered. The left panels are inside the AFe phase, and show a spectral distribution at the chemical potential that corresponds to a small, electron-like Fermi surface. On the contrary, the right panels (the top one inside the AFh phase and the bottom one in the PM region) indicates a larger Fermi surface that still contains  $f$  electrons at that value of temperature  $T$ . We note the signals of shadow bands in the anti-ferromagnetic  $A(k)$  of the top panel and left bottom one.

### 3.5. Why Fermi surface reconstruction?

In order to better clarify whether the Fermi surface reconstruction is due to the onset of magnetic order or not, we carry on with variational calculations trying to uncover features that indirectly signal the  $f$  electron localization. In fact, in the variational phase diagram of Fig. 3.10 the onset of magnetism is not necessarily accompanied by the Fermi surface reconstruction. Viceversa, one could speculate that the latter might not require magnetism, which would be the case if the Fermi surface changes were caused by the  $f$  electron localization [71]. This issue has been addressed theoretically in the periodic Anderson model [72]. Here, we investigate the simplest paramagnetic wave function, with neither superconductivity nor magnetism. Clearly, having only the hybridization  $V$  and the chemical potential  $\mu_f$ , the topology of the band structure does not change by varying  $J$ . Therefore, at first sight, one would not expect to find anything special in the paramagnetic sector. Nevertheless, even in this case, we do observe a critical  $J$  at which the momentum dependent spectral function  $A(k)$  of the conduction electrons at the chemical potential changes. Indeed, while at zero temperature the Fermi surface does not change with  $J$ , a small but finite value of  $T$  produces non-trivial features connected with the magnitude of matrix elements of Eq.(3.28). For  $J \gtrsim 0.5$ , the Fermi surface includes the  $f$  electrons, while, below it does not, see Fig. 3.16. This is very similar to the behavior that we found when magnetism is also

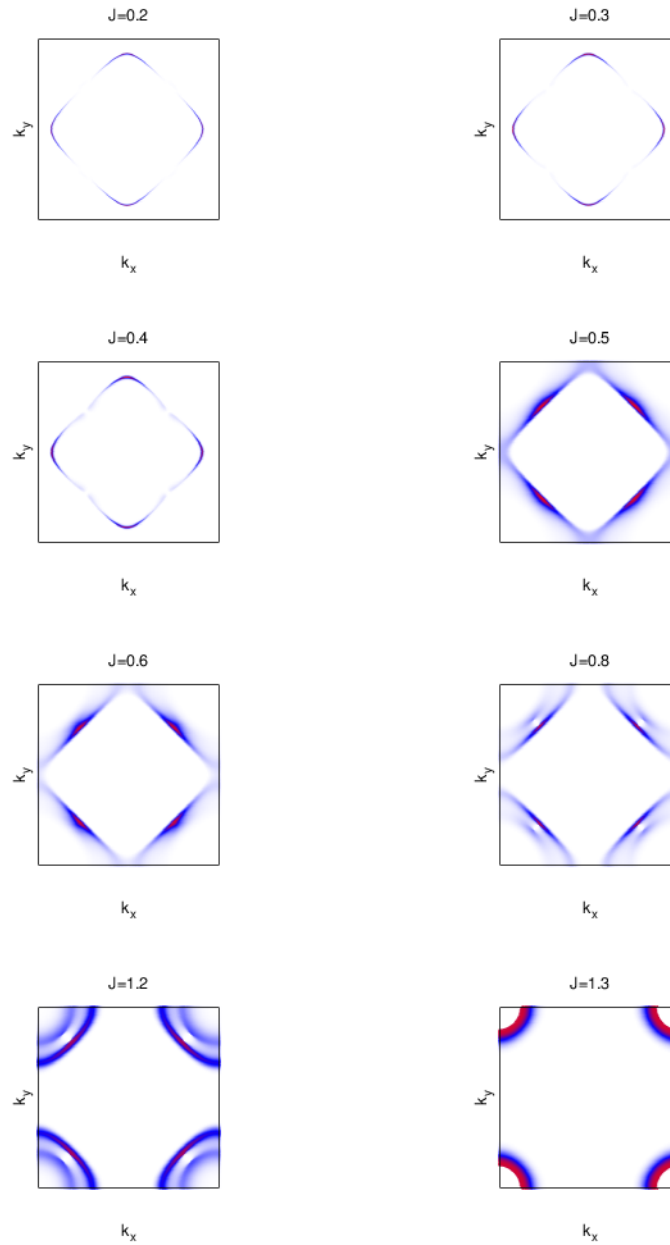


Figure 3.14.: Emission spectrum  $A(k)$  broadened with a temperature  $T = 0.01$  for  $n_c = 0.91$ . The values of  $J < 1.3$  are inside the  $d$ -wave superconducting dome, while  $J = 1.3$  is already in the metallic phase. Note the change of topology as  $J$  increases.

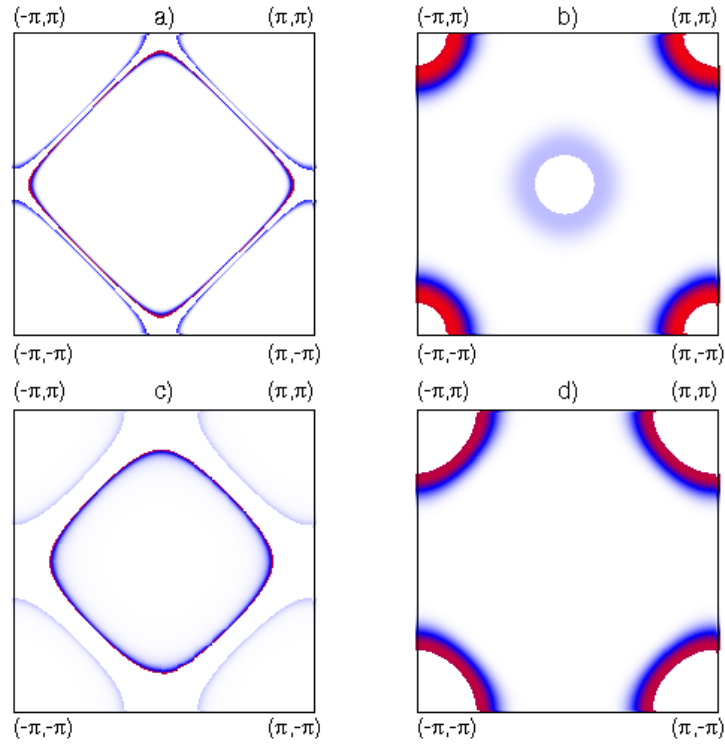


Figure 3.15.: Emission spectrum  $A(k)$  broadened with a temperature  $T = 0.01$ . Top left panel:  $n_c = 0.93$  and  $J = 0.3$ , inside the AFe phase. Top right panel:  $n_c = 0.93$  and  $J = 1.3$ , inside the AFh phase. Bottom left panel:  $n_c = 0.75$  and  $J = 0.2$ , inside the AFe phase. Bottom right panel:  $n_c = 0.75$  and  $J = 1.2$ , inside the PM phase. Note the shadow bands for the antiferromagnetic cases.

present. However, this change occurs now not because the band structure is modified but because the spectral weight of the conduction electrons at the Fermi energy changes. Indeed, looking carefully at the momentum distribution, one can distinguish two sheets of the Fermi surface: a small one, which corresponds to the non-interacting conduction electrons Fermi surface, and a large one that includes also the  $f$  electrons. Across the crossover, the relative weights of these two sheets is modified quite sharply. This behavior can be regarded as a manifestation of  $f$  electron localization. Moreover, by the inspection of Kondo and kinetic terms separately, we highlight the fact that a large Fermi surface is favored by large Kondo exchange, while a small Fermi surface implies a large kinetic energy for conduction electrons, see Fig. 3.17. This suggests that the modification of the Fermi surface is primarily due to the competition between the kinetic term and the Kondo exchange, and not between Kondo and RKKY interactions, as frequently invoked.

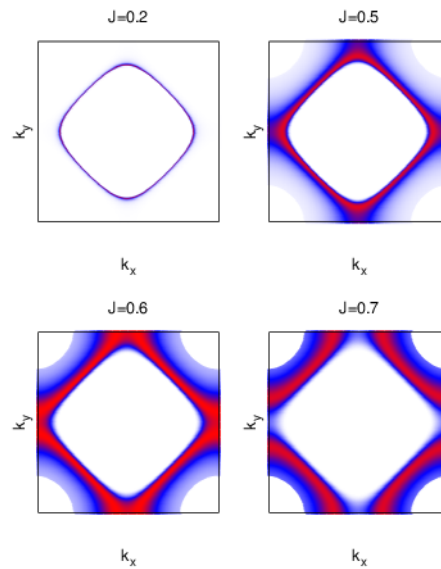


Figure 3.16.: Emission spectrum  $A(k)$  broadened with a temperature  $T = 0.01$  in the paramagnetic sector at  $n_c = 0.75$  for different values of  $J$ .

Therefore, the transition lines in the final phase diagram of Fig. 3.10 could be explained in the following way. The first-order line that separates the paramagnet from the AFe phase is primarily due to  $f$  localization, magnetism being just its by-product. On the contrary, the second-order line close to the compensated regime  $n_c = 1$  is more likely to be interpreted as a Stoner's instability of the paramagnetic Fermi liquid, driven by the nesting property of the Fermi surface. Across this second-order phase transition, the Fermi surface changes smoothly following the splitting of the bands.

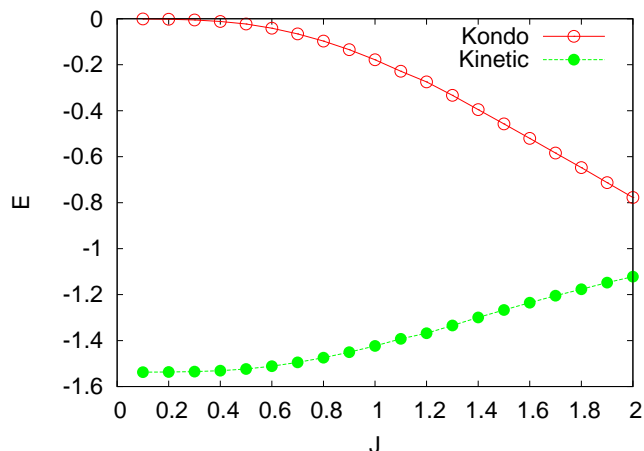


Figure 3.17.: Behavior of Kondo and kinetic energy terms for  $n_c = 0.75$  in the paramagnetic phase.

### 3.6. Conclusion

In this chapter, we studied the Kondo lattice model on a square lattice by mean-field approximation and VMC technique. The mean-field phase diagram is qualitatively similar to the variational Monte Carlo one. A wide region of the mean-field phase diagram is covered by AFs phase, while in the VMC one is replaced by AFe. This is due to the Gutzwiller projection, which imposes exactly one  $f$  electron per site in the VMC scheme and gives also good estimate of the ground-state energy. Both in mean-field and VMC, for  $n_c > 0.81$  there are two transitions: by decreasing  $J$ , the first one is continuous and connects a paramagnetic state to the AFh phase; the second one is first order and separates two magnetically ordered phases, i.e., AFh and AFe. This is a topological phase transition in which the Fermi surface topology changes. For  $n_c < 0.81$  there is just one discontinuous phase transition between paramagnetic and AFe states. Here, the breakdown of Kondo screening happens exactly at the magnetic transition. We found that the change of the Fermi surface is not necessarily due to magnetism but is due to  $f$  localization, magnetism being of one of its by-products.

At the mean-field level, pairing correlations are not found, since the only pairing order parameter that arises from decoupling of the exchange term is not independent from hybridization. Instead, thanks to the Gutzwiller projection, we found a large  $d$ -wave superconducting region in the paramagnetic sector. The  $d$ -wave symmetry of the superconductivity is similar to what has been observed in some heavy fermion compounds. When we allow for antiferromagnetism, the latter prevails over superconductivity, which disappears from the final phase diagram. We would like to mention that some evidence for a coexistence between magnetism and superconductivity has

been observed for small values of exchange coupling  $J$ ; however, the tiny condensation energy and the behavior of pair-pair correlations suggest that this fact might be only a finite size effect. Overall, in the variational phase diagram there is no superconducting phase. Therefore, in order to describe the observed superconducting phase in heavy-fermion materials, additional terms must be added in the simple KLM. In the next chapter we will undertake simple attempt and include adhoc frustration to investigate the emergence of pairing correlations in the final phase diagram.

## 4. Frustrated Kondo Lattice Model on 2D Lattice

The recent experimental observation that the antiferromagnetic transition and the small-to-large Fermi surface twist are separated has led to the proposal that frustration is an important ingredient in the heavy-fermion materials [73, 74]. Moreover, the introduction of frustration permits to study the physics of heavy-fermion materials in a broader perspective. The appearance of frustration in real heavy-fermion systems may take various forms. In certain cases, it can appear as a direct geometric frustration, as in the pyrochlore heavy fermion material  $Pr_2Ir_2O_7$  [75] and the Shastry-Shutherland lattice compound  $Yb_2Pt_2Pb$  [76]. Frustration can also take other forms, derived from competing interactions of various kinds. For example, in the heavy-fermion physics of bilayer  $^3He$  frustration may derive from ring-exchange effects in the lower almost localized layer of Helium atoms [77]. Recently, it has been investigated how frustration influences the quantum phase transition and the breakdown of Kondo effect after the magnetic transition. Remarkably, it has been claimed that a long-range electron hopping in the two-dimensional Kondo lattice model may enlarge the stability region of antiferromagnetism [78].

In the previous chapter, we studied the standard Kondo lattice model (KLM), with only nearest-neighbor hopping for conducting electrons and the main outcome was that superconductivity is possible only when the antiferromagnetic order is artificially switched off. Our final phase diagram does not contain any regime where a superconducting ground state is clearly stable. Nevertheless, the BCS wave function is competitive with magnetic states, suggesting that superconductivity (or at least a coexistence of magnetism and superconductivity) is possible when additional terms are added to the standard KLM. In this regard, the most natural ingredient that frustrates long-range magnetism but does not interfere with pairing is a next-nearest-neighbor hopping  $t'$  between conduction electrons. Indeed, a finite  $t'$  reduces the magnetic polarization at  $k = (\pi, \pi)$ , which is responsible for the indirect interaction among localized moments.

In the following, we analyze KLM in the two dimensional square lattice including the next-nearest-neighbor hopping, with particular emphasis on the possible appearance of superconductivity in the ground state.

## 4.1. The frustrated model and basic considerations

Here, we define the frustrated KLM by adding to the Hamiltonian of Eq.(3.1) a next-nearest-neighbor hopping, connecting the same sublattice on the square lattice:

$$H = -t \sum_{\langle i,j \rangle, \sigma} c_{i,\sigma}^\dagger c_{j,\sigma} - t' \sum_{\langle\langle i,j \rangle\rangle, \sigma} c_{i,\sigma}^\dagger c_{j,\sigma} + h.c + J \sum_i S_i \cdot s_i, \quad (4.1)$$

where the notation is standard; Fig. 4.1 shows the allowed hopping processes for conduction electrons of Hamiltonian of Eq.(4.1). The additional hopping  $t'$  is the origin of magnetic frustration. Before discussing the results of the frustrated KLM, it is in-

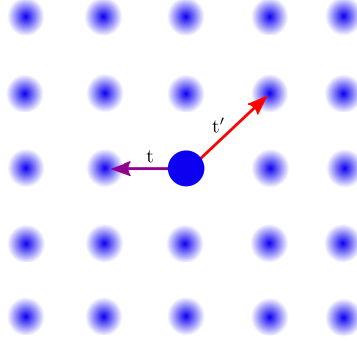


Figure 4.1.: Allowed hopping processes for the used two-dimensional lattice.

structive to show the effect of  $t'$  for non-interacting fermions on the two dimensional lattice. Indeed, a finite next-nearest-neighbor hopping lead to important modifications in the band structure. Let us consider the total density of states, which is defined by:

$$Dos(E) = \sum_k \delta(E_k - E), \quad (4.2)$$

in which

$$E_k = -2t(\cos(k_x) + \cos(k_y)) - 4t' \cos(k_x) \cos(k_y) \quad (4.3)$$

is the band structure of free electrons on the square lattice. In Fig. 4.2, we show the density of states for few cases with positive and negative values of  $t'$ . It turns out that density of states for positive and negative  $t'$  are simply connected (they are mirror images of each other with respect to  $E = 0$ ). This can be easily understood by performing the canonical transformation

$$c_{i\sigma}^\dagger \rightarrow (-1)^{R_i} c_{i\sigma}, \quad (4.4)$$

which changes the sign of  $t'$  in the free Hamiltonian and the number of electrons from  $N_c$  to  $2N - N_c$ , where  $N$  is the number of sites.

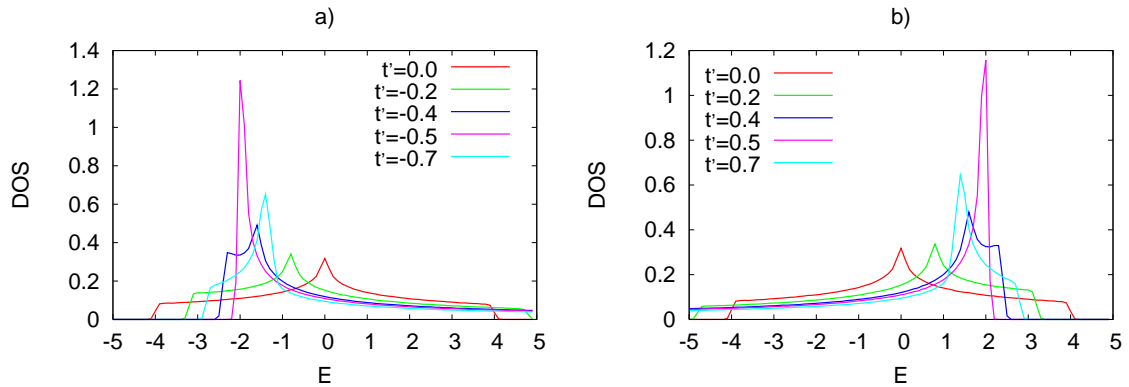
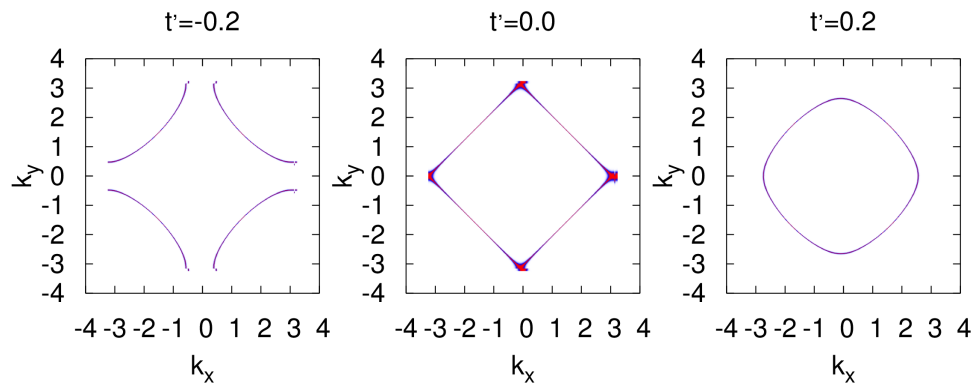


Figure 4.2.: Total density of states for free electrons on square lattice.

The presence of a finite next-nearest-neighbor hopping changes the overall energy spectrum and, therefore, has important effects on the shape of the Fermi surface. In Fig. 4.3 the emission spectrum (see Eq.(3.27)) for free electrons is plotted at the chemical potential and broadened with a small temperature  $T = 0.01$ . The case with  $t' = 0$  is also shown for a reference (see middle panel of Fig. 4.3). Positive and negative values of  $t'$

Figure 4.3.: Spectral function for free electrons on the square lattice with  $T = 0.01$  and  $n_c = 0.9$  for three values of  $t'$ .

modify the Fermi surface in different ways. The degeneracy between  $k = (\pm\pi/2, \pm\pi/2)$  and  $k = (\pi, 0)$  or  $(0, \pi)$  is removed; while for positive values of  $t'$ , the Fermi surface is closed (roughly speaking is “electron-like”), for negative ones, it is open (namely “hole-like”), see Fig. 4.3. This fact will have important consequences when including the Kondo term. For  $t' > 0$ , in contrast to the simple-minded expectation that frustration may suppress magnetism, we will find that the antiferromagnetic phase with an electronlike (i.e., small) Fermi surface extends its stability region. For  $t' < 0$ , instead

states with a large Fermi surface (including the paramagnetic one) are favored.

## 4.2. Positive next-nearest-neighbor hopping amplitude

As we discussed, different signs of  $t'$  for free fermions lead to different shapes of the Fermi surface. Therefore, when free fermions are hybridized with  $f$  local moments via the super-exchange Kondo interaction  $J$ , the ground state of the correlated system will also crucially depend on the value of  $t'$ . In this section, we start by investigating the effects of positive values of the next-nearest neighbor hopping on the ground state.

### 4.2.1. Paramagnetic sector

Here, we start by investigating the paramagnetic sector and show how the phase diagram is modified when a finite value of  $t' > 0$  is considered. In the following, we will take a cluster with 196 sites (i.e.,  $14 \times 14$ ). Unfortunately, given the presence of both conduction and localized electrons, larger sizes are very hard to be handled and will not be afforded here.

The paramagnetic wave function is constructed from the mean-field Hamiltonian:

$$H_{\text{PM}} = \sum_{k,\sigma} \begin{bmatrix} c_{k,\sigma}^\dagger & f_{k,\sigma}^\dagger \end{bmatrix} \begin{bmatrix} \epsilon_k + \epsilon_k^{\text{nnn}} & V \\ V & \epsilon_k^{\text{ff}} - \mu_f \end{bmatrix} \begin{bmatrix} c_{k,\sigma} \\ f_{k,\sigma} \end{bmatrix}, \quad (4.5)$$

which is similar to the one considered for the unfrustrated KLM, see Eq.(3.19), but having one additional variational parameter, namely the next-nearest-neighbor hopping for conduction electrons  $t'_v$  in the kinetic term

$$\epsilon_k^{\text{nnn}} = -4t'_v \cos(k_x) \cos(k_y). \quad (4.6)$$

The inclusion of this variational parameter is indeed crucial to improve the final variational energy.

To allow for superconductivity, suitable pairing terms should be added in the Hamiltonian of Eq.(4.5), similarly to what have been discussed in the unfrustrated model. In real space, possible pairings are:

$$\Delta_{i,j}^{\text{ff}} = \langle f_{i,\uparrow}^\dagger f_{j,\downarrow}^\dagger + f_{j,\uparrow}^\dagger f_{i,\downarrow}^\dagger \rangle, \quad (4.7)$$

$$\Delta_{i,j}^{\text{cc}} = \langle c_{i,\uparrow}^\dagger c_{j,\downarrow}^\dagger + c_{j,\uparrow}^\dagger c_{i,\downarrow}^\dagger \rangle, \quad (4.8)$$

$$\Delta_{i,j}^{\text{cf}} = \langle c_{i,\uparrow}^\dagger f_{j,\downarrow}^\dagger + f_{j,\uparrow}^\dagger c_{i,\downarrow}^\dagger \rangle. \quad (4.9)$$

In the following, we consider both on-site ( $i = j$ ) and extended pairing (nearest-neighbor) with  $s$ - or  $d$ -wave symmetries.

The correlated variational states are obtained by including the Gutzwiller projection in order to enforce the single occupancy of the  $f$  electrons. Then, we use variational Monte Carlo technique to minimize the ground-state energy with and without pairing correlations for different values of  $t'$ . In the presence of frustration, we find a quite extended region with  $d$ -wave superconductivity (similarly to the non-frustrated case). Fig. 4.4 shows the energy difference of the superconducting state with respect to the paramagnetic one for the conduction electron density  $n_c = 0.93$  and different values of  $t'$ .

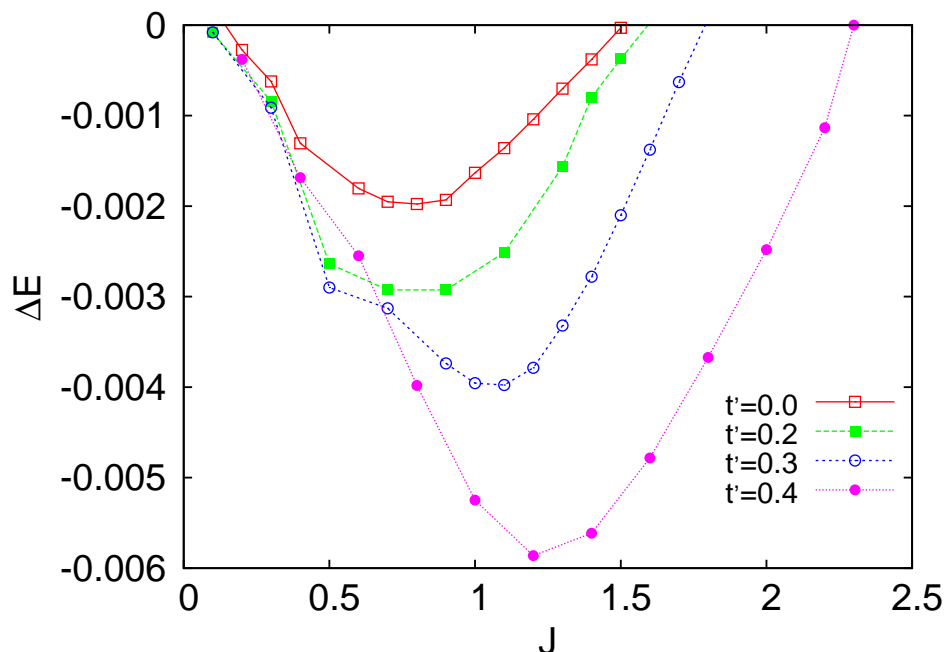


Figure 4.4.: Energy difference between the normal and the superconducting states as a function of the exchange coupling  $J$  for different  $t' > 0$ . The density of conduction electrons is  $n_c = 0.93$ .

Remarkably, the presence of a finite next-nearest-neighbor hopping considerably enhances the condensation energy. Indeed, while for  $t' = 0$  the maximum gain is  $\Delta E = -0.002$ , for  $t' = 0.4$  we obtain  $\Delta E = -0.006$ . We also notice that the value of  $J$  which the maximum gain occurs increases with  $t'$ . The other interesting aspect is that frustration enlarges the stability of the superconducting phase, up to quite large values of  $J$ : the critical  $J$  at which superconductivity disappears is 1.5 for  $t' = 0$  and 2.4 for  $t' = 0.4$ . The stabilization of superconductivity for large values of the Kondo super-exchange is remarkable and may lead to a true superconducting phase in the actual phase diagram, even when antiferromagnetism is included.

### 4.2.2. Antiferromagnetic sector

Let us now consider antiferromagnetism and compare magnetic and paramagnetic (superconducting) states. The antiferromagnetic wave function is constructed from the mean-field Hamiltonian of Eq.(3.24) but also including variational next-nearest-neighbor  $t'_v$ . In this case a perfect nesting is no longer present:

$$E_{k+Q} \neq -E_k \quad (4.10)$$

where

$$E_k = -2t[\cos(k_x) + \cos(k_y)] - 4t' \cos(k_x) \cos(k_y) \quad (4.11)$$

and  $Q = (\pi, \pi)$ . Similarly to the unfrustrated case, also in the presence of a finite next-nearest-neighbor hopping, three possible magnetic states can be obtained, having different Fermi-surface topologies, i.e., AFe, AFh, and AFs.

In Fig. 4.5, we report our calculations for the energy of different states, compared to the non-superconducting paramagnetic state for different values of  $t'$  and  $n_c = 0.93$ . The non-frustrated case of the previous chapter has been also included for comparison. The first important outcome is that the AFh state is strongly penalized by including  $t'$ . Indeed, its energy difference with respect to the paramagnetic state decreases by increasing  $t'$ . On the contrary, the AFe state is able to take advantage of the presence of a frustrating hopping, leading to a quite substantial energy gain. As a result, while in the unfrustrated case there are two transitions when decreasing the Kondo exchange  $J$ , one from the paramagnetic phase to AFh and another one from AFh to AFe, in the presence of a sizable  $t'$ , a unique transition appears, between the paramagnet and the AFe phase.

Most importantly, the superconducting state easily takes over the AFh phase (especially for large values of  $J$  and  $t'$ ), leading to a true superconducting phase in the vicinity of the (first-order) transition between the paramagnet and the antiferromagnet. Indeed, the inclusion of the frustrating hopping enlarges the stability of both superconducting and AFe phases to larger values of  $J$ . Eventually, a sizable region with superconducting order is found, e.g., for  $t' = 0.4$  and  $2 < J < 2.4$ , see Fig. 4.5.

We have also considered different electron densities, further away from the compensated regime. In Fig. 4.6 the energy differences of the superconducting and the AFe states with respect to paramagnetic state have been reported for  $n_c = 0.8$  for  $t' = 0.4$ . In this case, although the condensation energy of the superconducting phase is enhanced with respect to the unfrustrated regime, the AFe state always gives a better solution. Therefore, for small concentrations of the conducting electrons, the final phase diagram is similar to the non-frustrated one (although the critical value for the first-order transition depends upon  $t'$ ). In this regime of fillings, the transition is such that both the

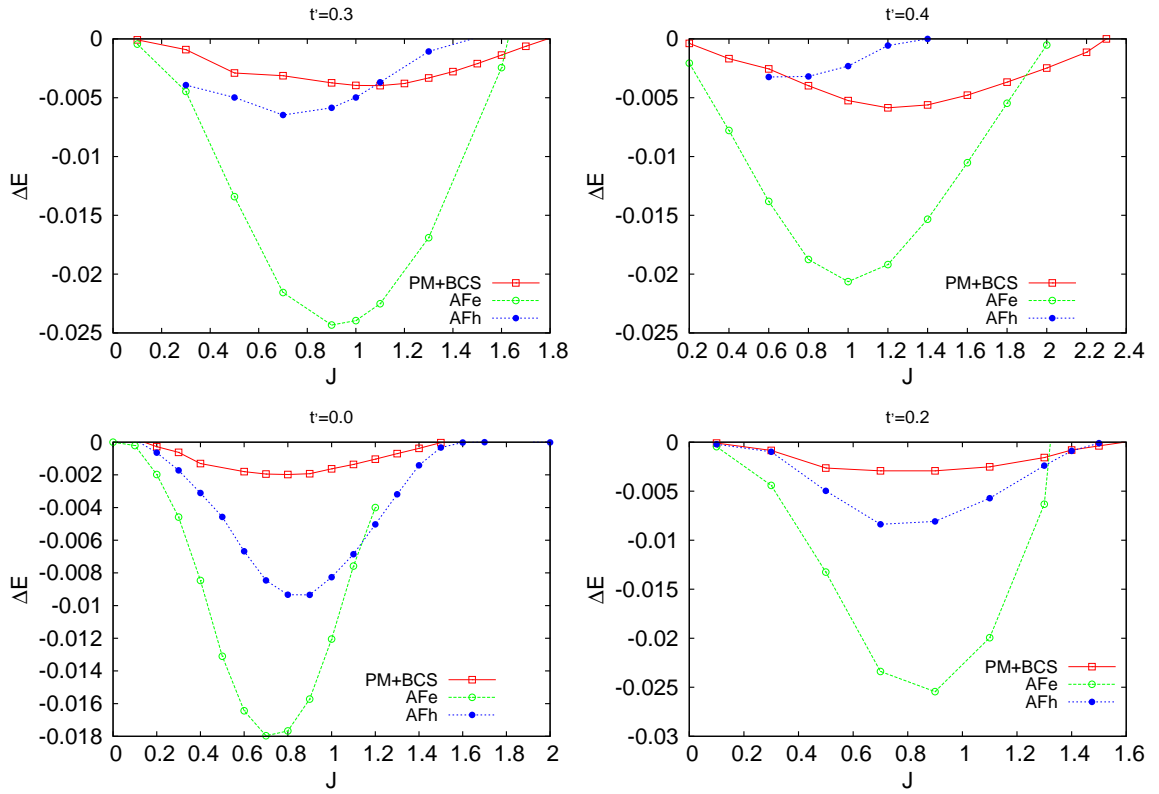


Figure 4.5.: Energy difference of magnetic and superconducting phases with respect to paramagnetic state as a function of the exchange coupling  $J$  for different  $t' > 0$ . The density of conduction electrons is  $n_c = 0.93$ .

occurrence of magnetism and the Kondo breakdown happen at the same point.

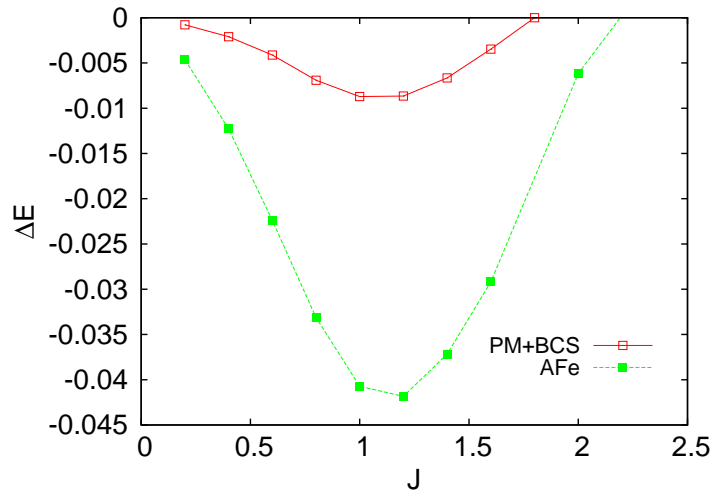


Figure 4.6.: Energy difference with respect to paramagnetic state as a function of the exchange coupling  $J$  for  $t' = 0.4$ . The density of conduction electrons is  $n_c = 0.8$ .

### 4.3. Negative next-nearest-neighbor hopping amplitude

In this section, we study the frustrated Hamiltonian of Eq.(4.1) for negative values of the next-nearest-neighbor hopping, i.e.,  $t' < 0$ . Also in this case, we are interested in the existence of superconductivity in the ground-state phase diagram, especially close to the magnetic transition. The variational wave functions are constructed similarly to the case with  $t' > 0$ .

First we concentrate on the paramagnetic sector. In the Fig. 4.7, the condensation energy of the superconducting state is reported for different values of  $t'$  and  $n_c = 0.93$ . In contrast to the previous section, a negative value of  $t'$  strongly suppresses the superconducting condensation energy, which decreases by increasing  $t'$ . The maximum gain of  $\Delta E = -0.002$  in the non-frustrated case becomes  $\Delta E = -0.0008$  for  $t' = -0.4$ . In the frustrated system also the region of stability for the superconducting state is reduced. This is particularly evident for small values of the Kondo super-exchange: while for the non-frustrated case the BCS state remains stable down to very small  $J$ 's, for  $t' = -0.4$  there is a critical value  $J \simeq 0.4$  under which no superconductivity is present. We would like to notice that the small condensation energy that has been obtained for large  $t'$  is not due to finite-size effects and represents a genuine behavior of the frustrated KLM.

To go beyond, we consider antiferromagnetism inside the variational states. In

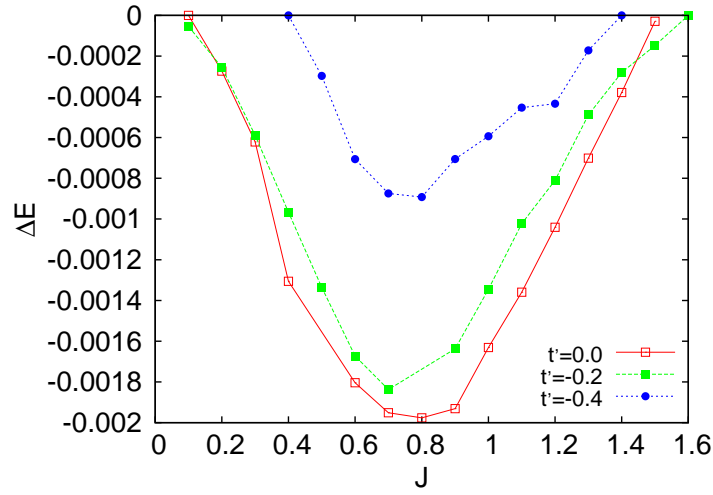


Figure 4.7.: Energy difference between the normal and the superconducting states as a function of the exchange coupling  $J$  for different  $t' < 0$ . The density of conduction electrons is  $n_c = 0.93$ .

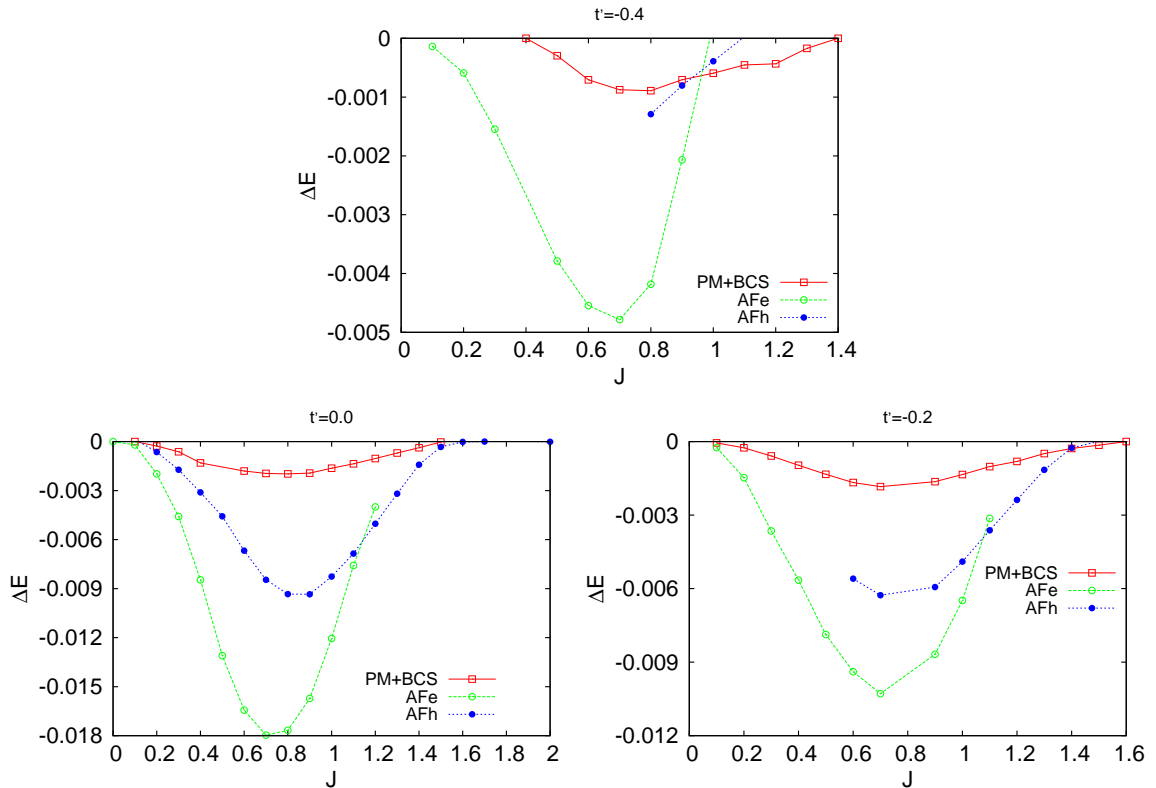


Figure 4.8.: Energy difference of magnetic and superconducting phases with respect to paramagnetic state as a function of the exchange coupling  $J$  for different  $t' < 0$ . The density of conduction electrons is  $n_c = 0.93$ .

Fig. 4.8, we report the results of the energy difference with respect to a paramagnetic metal for all magnetic and superconducting states at  $n_c = 0.93$  and various  $t'$ . In contrast to the case with a positive frustrating hopping, here  $\Delta E$  is suppressed for all phases, even the ones with magnetic order. In particular, the AFh state has the strongest decrease, which ends up to its disappearing from the phase diagram. Most importantly, this fact leads to a region in which superconductivity takes place for large enough values of  $t'$ , i.e.,  $t' = -0.4$ , see Fig. 4.8. However, it should be noticed that the condensation energy is much smaller (one order of magnitude) than the case with positive  $t'$ , e.g.,  $\Delta E \simeq -0.0005$  versus  $\Delta E \simeq -0.005$ . Therefore, we expect that BCS superconductivity is much more fragile in this case and could be washed out by small perturbations.

Finally, similarly to what has been obtained for positive  $t'$ , at small densities the AFe phase always overcomes the superconducting one, leading to a first-order transition between a paramagnetic state without pairing and an antiferromagnetic state with a small Fermi surface.

We mention that the results for  $t' > 0$  can be mapped to those for  $t' < 0$  with  $n_c \rightarrow 1 - n_c$ . This is to emphasize that the results shown in the following for  $n_c < 1$  for  $t' > 0$  and  $t' < 0$  are actually fully general.

#### 4.4. Final variational phase diagram and conclusions

In this Chapter, we studied the effect of frustration in the two-dimensional Kondo lattice and investigated both negative and positive  $t'$ . In Fig. 4.9 we show the schematic phase diagram that is obtained by using variational Monte Carlo approach that includes the strong correlation between  $f$  electrons. This picture equally represents both negative and positive values of frustration. In the case of  $t' > 0$ , the magnetic transition is clearly first order, because of the reconstruction of the topology of the Fermi surface, which changes from large to small when entering into the magnetic phase. On the other side, for  $t' < 0$  the fate of the magnetic transition for large frustrations is not clear: a small region with AFh may indeed intrude between the paramagnetic and the AFe phases, even though with a fragile condensation energy, see Fig. 4.8. Most importantly, for  $n_c \gtrsim 0.8$ , a superconducting solution may be stabilized in the vicinity of the magnetic transition, with a large condensation energy for positive values of  $t'$ . For small densities of conduction electrons  $n_c \lesssim 0.8$ , there is no superconductivity and the phase diagram closely resembles the unfrustrated one, with a unique magnetic transition between a paramagnetic metal and an antiferromagnet with a small Fermi surface. As a final remark, we would like to emphasize that a positive value for the frustrating hopping favors superconductivity, while a negative one strongly suppresses the condensation energy.

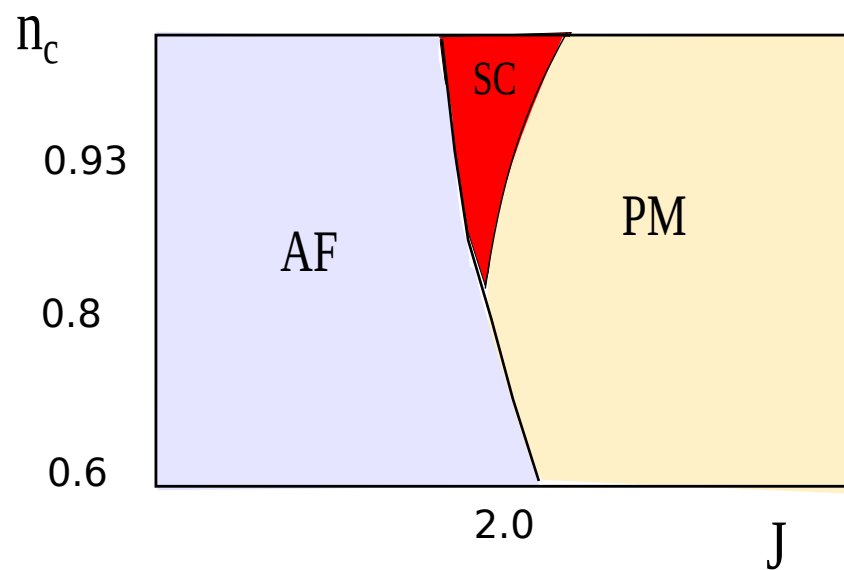


Figure 4.9.: Schematic phase diagram of frustrated Kondo on the two-dimensional square lattice. The picture is valid for both large enough positive and negative value of  $t'$ .



## 5. Kondo Heisenberg Model on 2D Lattice

In chapter 3 we have found that the phase diagram of the simplest version of the Kondo lattice model (KLM) does not comprise a superconducting phase at the border of the paramagnetic-to-antiferromagnetic quantum critical point, as often observed in real heavy-fermion materials. Although we cannot exclude that this fact arises because of the low dimensionality of the model, we think it is more likely that the simple KLM is too simplified to reproduce all phases encountered experimentally. Indeed, we already showed that it is sufficient to add magnetic frustration to stabilize a superconducting dome. Another ingredient that one could add without making the model too involved is a direct magnetic exchange between the  $f$  local moments. In general, one expects that local moments are mutually coupled mostly via the RKKY interaction, i.e., through the spin-polarization of the conduction sea. However, the class of variational wave functions that we are able to deal with is not able to fully capture the RKKY mechanism. Indeed this would require  $SU(2)$  spin-spin correlations inside the Jastrowfactor, which is practically impossible within our variational Monte Carlo. One way to bypass this problem, though not rigorous, is by adding an explicit exchange among the local moments that mimics the RKKY coupling, which we are going to do in this chapter. Even though such an exchange is mainly a trick to include RKKY interaction effects otherwise missing in the variational wave function, it is not unlikely that a direct  $f$ - $f$  exchange of sizable magnitude does exist in some materials.

### 5.1. Kondo Heisenberg lattice model

The antiferromagnetic Kondo Heisenberg lattice model (KHLM) is given by:

$$H = -t \sum_{\langle i,j \rangle, \sigma} c_{i,\sigma}^\dagger c_{j,\sigma} + h.c + J \sum_i S_i \cdot s_i + J_H \sum_{\langle i,j \rangle} S_i \cdot S_j, \quad (5.1)$$

where  $J_H > 0$  is an antiferromagnetic nearest-neighbor exchange among the localized spins-1/2 (see Fig. 5.1), and the rest of the Hamiltonian is similar to the one described in section 3.1.

Previous investigations already suggested that, e.g., in the case of  $UPd_2Al_3$ , the antiferromagnetic coupling between localized spins is important to understand the superconducting phase [79]. Moreover, other authors already remarked the importance

of  $J_H$  when focusing on the magnetism of heavy fermions [76, 80, 81, 30, 9, 82, 83]. We also note that the same KHLM is supposed to describe manganites when  $J < 0$

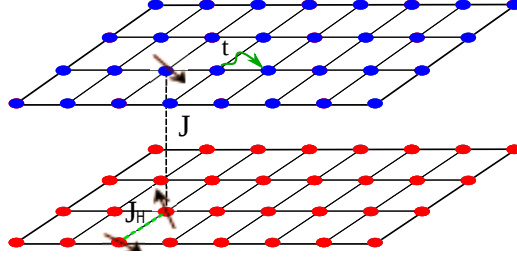


Figure 5.1.: A schematic representation of the Kondo Heisenberg lattice model. There are two species of electrons: the conduction ones, which live in the upper lattice, and the localized ones, which live in the lower lattice. The conduction electrons have a nearest-neighbor hopping with amplitude  $t$ ; conduction and localized electrons interact through the super-exchange coupling  $J$ . There is a direct antiferromagnetic interaction between local spins through exchange  $J_H$ .

corresponds to the Hund's Coulomb exchange [84]. Indeed, investigations of models for manganites have shown that  $J_H$  is crucial for the numerical stabilization of experimentally known phases that otherwise become unstable due to the strong ferromagnetic tendencies [84, 85]. Apart from the possible existence of a sizable  $f$ - $f$  direct exchange, we already mentioned that  $J_H$  also serves to enforce the RKKY interaction, though limited to nearest neighbors and with an antiferromagnetic sign consistent only to a conduction electron density not too far from the compensated regime  $n_c = 1$ .

In the following we shall investigate the Hamiltonian of Eq.(5.1) both in the paramagnetic and antiferromagnetic sectors and examine the role of  $J_H$  for the stabilization of superconductivity in the phase diagram.

## 5.2. Paramagnetic sector

We start by studying the paramagnetic sector allowing for superconductivity. We recall that the standard KLM with  $J_H = 0$  has already a large region with  $d$ -wave pairing correlations in the paramagnetic sector (see phase diagram in Fig. 3.6). The question we shall address is how a finite  $J_H > 0$  influences superconductivity.

As variational wave function we use the one described in section 3.3 with similar variational parameters. The correlated variational state is obtained by including the Gutzwiller projection to enforce the single occupancy of the  $f$  electrons. Then, we use variational Monte Carlo technique to minimize the ground-state energy with and without pairing correlations for different values of  $J_H$ . In the following, we will consider clusters with different sizes, e.g., from 64 to 196 sites. Since part of the RKKY

interaction is already built into the  $J_H = 0$  model, we choose very small values of  $J_H$  to avoid double counting. In Fig. 5.2, we show the energy difference of the superconducting state with respect to the paramagnetic one for different values of  $J_H$  at  $n_c = 0.93$ . The case of  $J_H = 0$  has been reported for comparison. Interestingly the maximal gain always remains peaked around  $J = 0.5$ , and it increases monotonically with  $J_H$ . Surprisingly, even a small  $J_H$  substantially enhances the condensation energy, which at  $J_H = 0$  is  $\Delta E \simeq 10^{-3}$  while already for  $J_H = 0.1$  becomes  $\Delta E \simeq 10^{-2}$ . In Fig. 5.2, the condensation energy at fixed values of  $J$  is plotted versus  $J_H$ , showing the linear dependence on  $J_H$ . The insertion of a finite  $J_H$  not only enlarges the condensation energy but also the stability region of superconductivity. While  $J_H = 0$  the transition to a normal metal occurs at  $J \simeq 1.5$ , for  $J_H = 0.1$  we obtain that superconductivity is stable up to  $J \simeq 2.2$ .

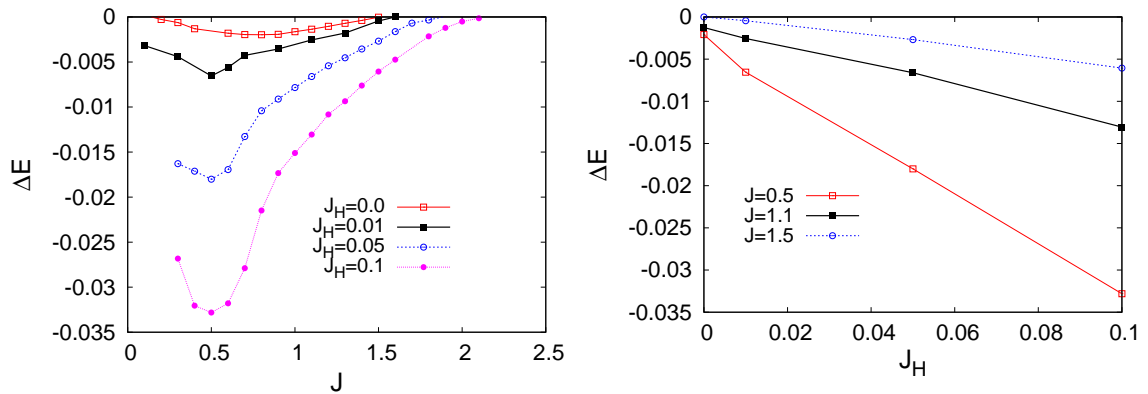


Figure 5.2.: Left panel: superconducting condensation energy versus the Kondo exchange  $J$  for different values of  $J_H$  at  $n_c = 0.93$ . Right panel: the same quantity for fixed value of  $J$  versus  $J_H$ .

To better illustrate the enhancement of pairing due to  $J_H$ , we compute the pair-pair correlations of Eq.(3.25). In Fig. 5.3 we report the results for the correlated BCS wave function for different values of  $J_H$  for  $J = 1.1$ . The non-interacting fermion case is also reported for reference. We observe that in the superconducting phase the behavior of correlations versus distance remains pretty constant in space and robust with an increasing value by increasing  $J_H$ . In conclusion, the phase diagram in the paramagnetic sector remains similar to the one for KLM with an extended region of  $d$ -wave superconductivity. The robust enhancement and extension of the BCS region could provide a chance for a superconducting ground state to appear in the final variational phase diagram. To address this issue we must allow for antiferromagnetism, which we do in what follows.

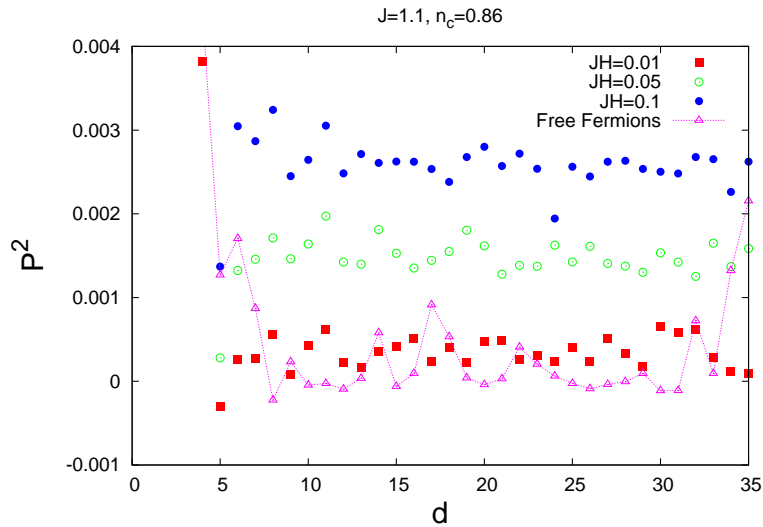


Figure 5.3.: Pair-pair correlations as a function of distance for  $n_c = 0.86$ ,  $J = 1.1$ , and different values of  $J_H$ . The correlations of free electrons are also reported for comparison.

### 5.3. Antiferromagnetic sector

Now, we also allow for magnetic states and consider three different wave functions with different Fermi surface topologies, i.e., AFs, AFe, AFh. As before, these antiferromagnetic wave functions are constructed from the mean-field Hamiltonian of Eq.(3.24). By using the variational Monte Carlo, we optimize the energy of each state and compare it with the paramagnetic and superconducting ones.

Obviously, a direct antiferromagnetic interaction  $J_H$  enhances the tendency towards Néel ordering, hence enlarges the stability region of antiferromagnetism. In Fig. 5.4, we show the calculations for the energy of different states, compared to the paramagnetic state for different values of  $J_H$  and  $n_c = 0.93$ . The case of the KLM, i.e.,  $J_H = 0$ , has been also included for comparison. Interestingly, even though  $J_H$  sustains antiferromagnetism, upon increasing  $J_H$  we do find a superconducting phase that finally gets energetically more favorable than AFh. In other words, a superconducting region right after the magnetic quantum critical point emerges thanks to the finite  $J_H$ . This behavior has a close resemblance to experimental phase diagrams of heavy fermions. Furthermore, by allowing the explicit presence of  $J_H$  also affects the pairing correlations within the magnetic sector. Indeed, by increasing  $J_H$  there is a robust enhancement of the coexistence of pairing and magnetism, both in the AFe phase as well as in the AFh one right after the first order topological transition from AFe to AFh. The region of superconductivity in the AFh phase is connected to the superconducting phase in the paramagnetic sector for large enough values of  $J_H$ . To better show the enhancement of

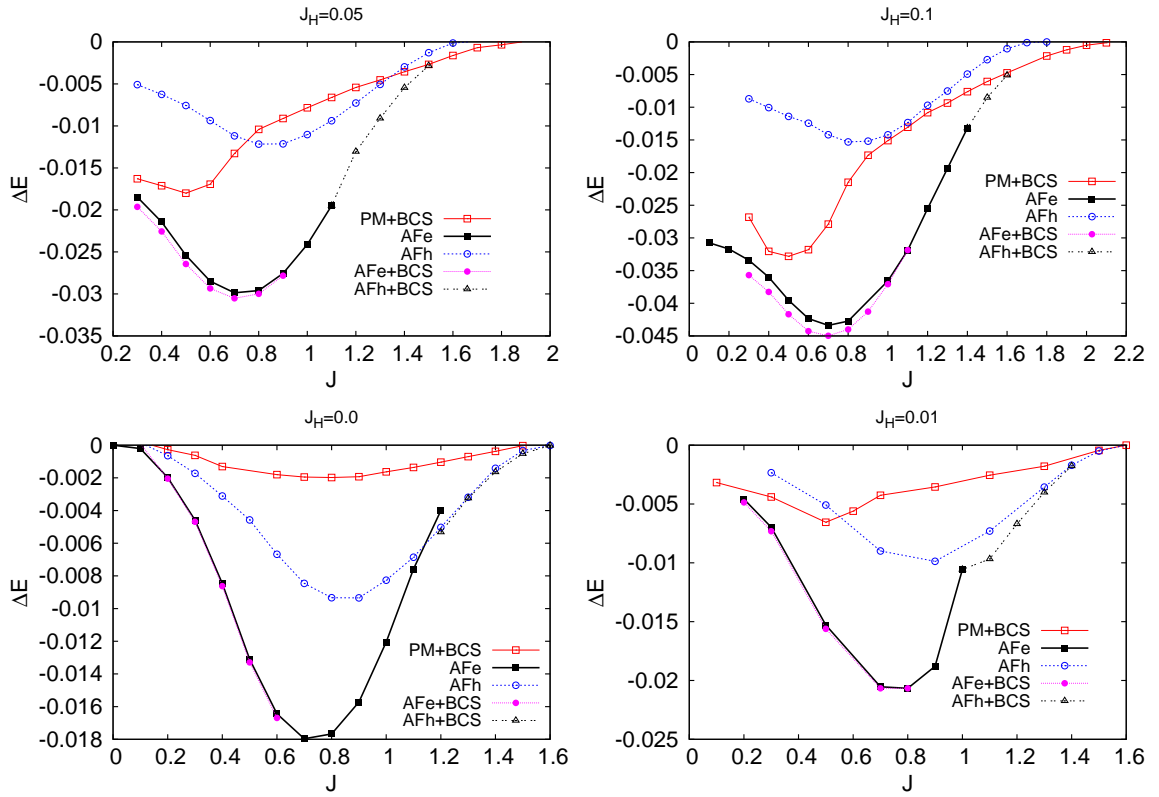


Figure 5.4.: Energy difference of magnetic and superconducting phases with respect to paramagnetic state as a function of the Kondo exchange  $J$ , for different values of  $J_H$  at  $n_c = 0.93$ .

superconductivity in the magnetic sector, we plot in Fig. 5.5 the condensation energy in the magnetic sector, i.e., the energy difference between the state with coexisting magnetism and superconductivity and the state with magnetism alone, for different values of  $J_H$ . The large energy gain in the AFh state due to electronic pairing is remarkable and indicates the robust existence of superconductivity in the proximity of the quantum critical point between paramagnetic and antiferromagnetic phases (see Fig. 5.4).

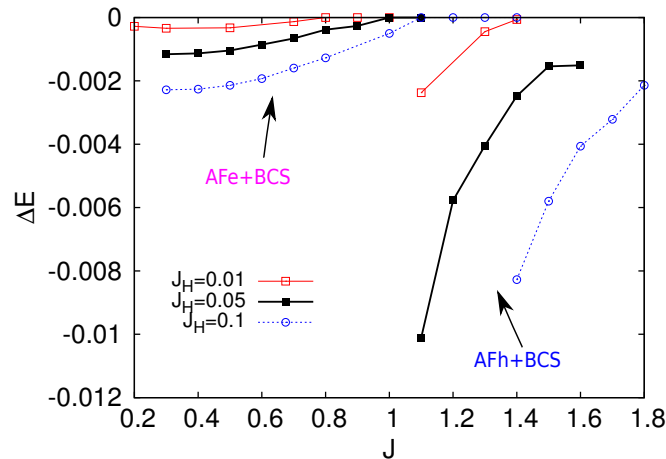


Figure 5.5.: Energy difference of the mixed state with both superconductivity and magnetism with respect to the state with only magnetism, for different values of  $J_H$  and  $n_c = 0.93$ .

Finally, we move to lower electron densities. Similarly to the  $J_H = 0$  case, when  $n_c \lesssim 0.8$  we cannot stabilize anymore an AFh phase. In Fig. 5.6 we show the energy differences of the various ordered phases with respect to the normal paramagnet one for  $J_H = 0.1$  and  $n_c = 0.64$ . We observe that the pure superconducting phase is now covered by the AFe state; however, now we find that there is a huge regime in which superconductivity coexists with antiferromagnetism. This is found not close to the (first-order) transition where magnetism takes place, but slightly inside the ordered phase.

## 5.4. Final phase diagram and conclusions

Here, we draw our ground-state phase diagram for  $J_H = 0.1$  in Fig. 5.7. A quite rich and interesting scenario is obtained. For electron densities close to the compensated regime  $n_c = 1$ , the paramagnetic metal becomes superconducting when  $J$  is decreased, just before the (second-order) magnetic phase transition. Moreover, a finite regime of coexistence between magnetism and superconductivity for both AFe and AFh states is found when the Kondo super-exchange is further decreased. For lower electron densities,

the pure superconducting phase disappears from the phase diagram; however, a mixed phase with both superconductivity and magnetism (with a small Fermi surface) is still present, for small enough Kondo couplings. We conclude by noting that the presence of  $J_H$  enhances at the same time both antiferromagnetism and superconductivity, thus indicating the importance of magnetic fluctuations for raising pairing correlations.

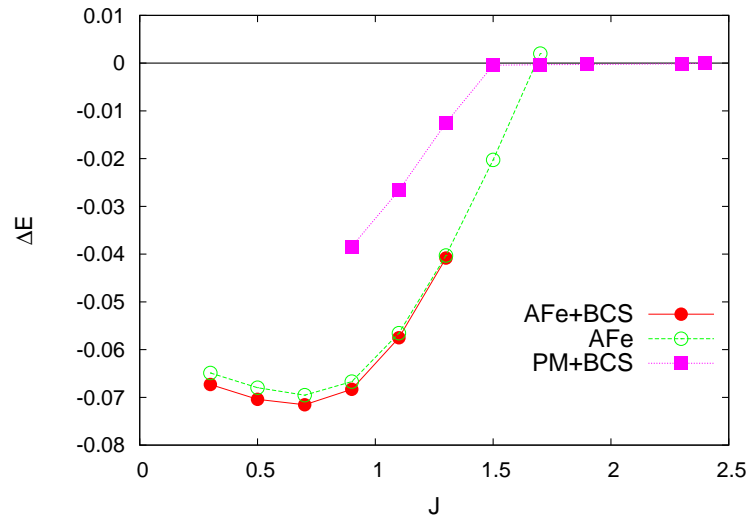


Figure 5.6.: Energy difference of the superconducting and magnetic phases with respect to the paramagnetic state for  $J_H = 0.1$  and  $n_c = 0.64$ .

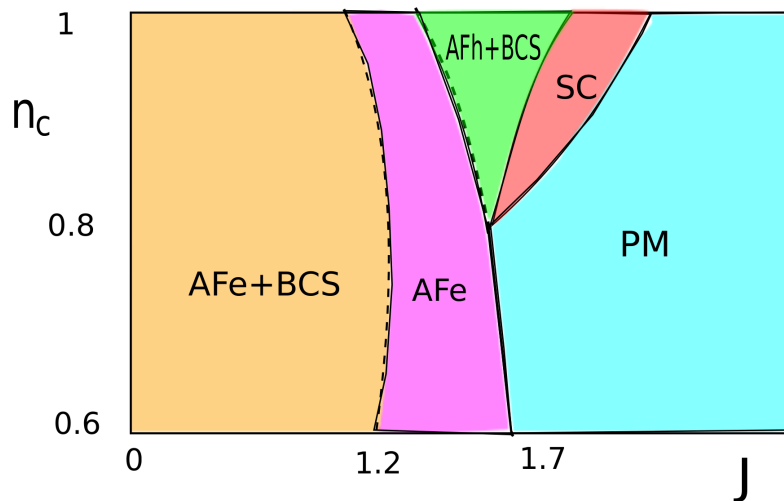


Figure 5.7.: Schematic phase diagram of the KHLM with  $J_H = 0.1$  as a function of  $J$  and  $n_c$ .



## 6. Summary

In this thesis we studied the Kondo lattice model on a square lattice at zero temperature by using numerical simulations based on variational Monte Carlo technique and simple Hartree-Fock approximation. We studied this model mainly to investigate the presence of any superconductivity in the phase diagram. At the mean-field level we did not find any superconducting solution. On the contrary, thanks to larger variational freedom of the Gutzwiller projected wave function with respect to the Hartree-Fock state, we did find by variational Monte Carlo a large region of  $d$ -wave superconductivity in the paramagnetic sector [86]. However, when we allowed for magnetism, the latter prevails over superconductivity which disappears from the phase diagram. Furthermore, we also found a small coexistence region of magnetism and superconductivity for small Kondo exchange coupling, but the tiny energy gain and the large-distance behavior of pair-pair correlations suggest this might be only a finite-size effect. We then had to conclude that the phase diagram of the Kondo lattice model does not include any superconducting region, at least within our variational approach limited to Gutzwiller projected wave functions.

To go beyond the above results, we added a new term to the Kondo lattice Hamiltonian [87]. Since in realistic materials there is always some degree of frustration, we mimicked it by a next-nearest-neighbor hopping  $t'$ . We investigated the effects of both negative and positive values of  $t'$ . Interestingly, for  $t' > 0$  we found a sizable enhancement of the pairing condensation energy in the paramagnetic sector, which pushes the stability region of superconductivity up to a quite large value of the Kondo exchange. When we then allowed for magnetism, we found, unlike before, that a superconducting region survives and intrudes between the antiferromagnetic and normal metal phases, at small and large Kondo exchange respectively, for conduction electron densities  $n_c > 0.8$ . The same also occurs when  $t' < 0$ , in which case, however, the condensation energy gain is much smaller than for  $t' > 0$ . For densities below  $n_c \lesssim 0.8$ , we could not find anymore superconductivity, hence the phase diagram becomes similar to that with  $t' = 0$ : an antiferromagnetic metal, with small Fermi surface, at weak Kondo exchange, separated by a first order transition from a paramagnetic heavy fermion metal, with a large Fermi surface, for stronger exchange.

We next studied the effects of a direct antiferromagnetic exchange  $J_H$  between the local moments. We found that  $J_H$  bring about a huge enhancement of the condensation

energy. The consequence is that, for  $J_H$  large enough superconductivity is stabilized in a small region between the antiferromagnet and the paramagnet and, like before, for  $n_c \gtrsim 0.8$ . We also have indications of regions of coexisting magnetism and superconductivity.

We finally note that the variational Monte Carlo phase diagram with  $t' \neq 0$  or  $J_H \neq 0$  bears a strong resemblance to the actual phase diagrams of many heavy-fermion compounds. We even could find a region of coexisting magnetism and superconductivity for  $J_H \neq 0$ , which is indeed observed in many of these compounds. Therefore, we should conclude that a Kondo lattice model that includes frustration and a direct antiferromagnetic exchange between the local moments produces a phase diagram that, within variational Monte Carlo, resembles more that of real heavy fermions. While adding frustration is physically conceivable, one may expect that realistic values of  $J_H$  should be fairly small to affect substantially the physics. However, we mention that our variational wave function, though better than any single Slater determinant, yet it does not fully account for the spin-spin correlations produced by the RKKY interaction. Therefore we believe that the explicit addition of  $J_H$  is a way to enforce directly in the Hamiltonian those missing effects.

## 7. Acknowledgement

I would like to express my special thanks of gratitude to my supervisors, Dr. Federico Becca and Prof. Michele Fabrizio who gave me the opportunity to do this wonderful project, which also helped me in doing a lot of research and I came to know about so many new things, I am really really thankful to them. I owe an extra thanks to Federico for his patience and continuous help, I would say he has been more than supervisor for me, thanks again Federico.

I would also like to thank my colleagues, Wenjun Hu, Riccardo Sabbatini and Simone Ziraldo for their useful discussion and help during my PhD. I owe a special thanks to Juan Felipe Carrasquilla who taught me how to parallelize the code. I would like also to thank Shahab Naghavi and Alwaleed Adllan who taught me many new things related to Linux and bash programming.

Thank to all the staff of SISSA for their hospitality and help during the years of my PhD.

I mention some of the great friends which I made during my PhD, they are at least: Luca, Ketty, Sanda, Vera, Corrado, Yabebal, Antonio, Masoud, Mahmoud, Milad, Shahab, Lara, Ben, Sogee, Georgette, Wenjun, Riccardo, Stefania, Nicola, Akbar, Alireza, Sahar, Maryam, Ariane, Elena, Alwaleed, Zhaleh, Fahimeh, Shima, Marjan, Sara, Najmeh, Mohammad, Mahrokh, Laleh, Saeed, Nader, Ladan, Houman, Fabian. YOU know who I mean and forgive me for not mentioning all great YOU, Thanks to all of YOU who made my stay and life in Trieste more pleasing.

THANKS AGAIN TO ALL WHO HELPED ME.



## A. Pair-pair correlations for free fermions on 2D lattice

Here in this section we will calculate the pair pair correlations for free fermions on 2D lattice. Hamiltonian for free fermions in momentum space is as follow:

$$H = \sum_{k\sigma} \epsilon_k c_{k\sigma}^\dagger c_{k\sigma} \quad (\text{A.1})$$

which on 2D they have the dispersion

$$\epsilon_k = -2t(\cos(k_x) + \cos(k_y)) \quad (\text{A.2})$$

The ground state for free electrons is described by fermi sea in which the band  $\epsilon_k$  has been filled up to the fermi momentum  $k_f$

$$\Psi = \prod_{k \leq k_f, \sigma} c_{k,\sigma}^\dagger |0\rangle \quad (\text{A.3})$$

If we expand the pair pair correlation of Eq. 3.25, it has four terms as follow:

$$\begin{aligned} & c_{j\downarrow} c_{i\uparrow} c_{l\uparrow}^\dagger c_{k\downarrow}^\dagger \\ & - c_{j\downarrow} c_{i\uparrow} c_{l\downarrow}^\dagger c_{k\uparrow}^\dagger \\ & - c_{j\uparrow} c_{i\downarrow} c_{l\uparrow}^\dagger c_{k\downarrow}^\dagger \\ & c_{j\uparrow} c_{i\downarrow} c_{l\downarrow}^\dagger c_{k\uparrow}^\dagger \end{aligned} \quad (\text{A.4})$$

After the Fourier transformation like below

$$c_{j,\sigma} = \frac{1}{\sqrt{L}} \sum_k e^{ik \cdot R_j} c_{k,\sigma} \quad (\text{A.5})$$

with  $L = L_x L_y$  be the lattice size and  $R_j$  is the location vector of electron at site  $j$ , for the first term of Eg. (A.4) we have:

$$c_{j\downarrow} c_{i\uparrow} c_{l\uparrow}^\dagger c_{k\downarrow}^\dagger = \frac{1}{L^2} \sum_{k_1, k_2, k_3, k_4} e^{ik_1 \cdot R_j} e^{ik_2 \cdot R_i} e^{-ik_3 \cdot R_l} e^{-ik_4 \cdot R_k} c_{k_1\downarrow} c_{k_2\uparrow} c_{k_3\uparrow}^\dagger c_{k_4\downarrow}^\dagger \quad (\text{A.6})$$

So by using of Wick theorem we have:

$$\langle c_{k_1\downarrow} c_{k_2\uparrow} c_{k_3\uparrow}^\dagger c_{k_4\downarrow}^\dagger \rangle_\Psi = \langle c_{k_4\downarrow}^\dagger c_{k_1\downarrow} \rangle_\Psi \langle c_{k_3\uparrow}^\dagger c_{k_2\uparrow} \rangle_\Psi = \delta_{k_1, k_4} \delta_{k_3, k_2} \quad (\text{A.7})$$

and then for the first term we get:

$$\langle c_{j\downarrow} c_{i\uparrow} c_{l\uparrow}^\dagger c_{k\downarrow}^\dagger \rangle_\Psi = \frac{1}{L^2} \sum_{k_1, k_2} e^{ik_1 \cdot (R_j - R_k)} e^{ik_2 \cdot (R_i - R_l)} \quad (\text{A.8})$$

By doing the same for the other three terms we finally get the following relation for  $P^2$ :

$$P_{ijkl}^2 = \frac{2}{L^2} \left[ \sum_{k_1 \leq k_f} e^{ik_1 \cdot (R_j - R_k)} \times \sum_{k_2 \leq k_f} e^{ik_2 \cdot (R_i - R_l)} + \sum_{k_1 \leq k_f} e^{ik_1 \cdot (R_j - R_l)} \times \sum_{k_2 \leq k_f} e^{ik_2 \cdot (R_i - R_k)} \right] \quad (\text{A.9})$$

As we see for free fermions pairing correlations decay as  $\frac{1}{L^2}$ . For a certain density of electrons  $n_c = N/L$  which determines  $k_f$  and specified boundary condition, given the sites  $i, j, k, l$  one could numerically calculate  $P^2$  from Eq. (A.9).

# Bibliography

- [1] K. Andres, J. Graebner, and H. R. Ott. *Phys. Rev. Lett*, 35:1779, 1975.
- [2] J. Kondo. *Prog. Theo. Phys*, 28:772, 1962.
- [3] T. Park and J. D. Thompson. *New J. Phys*, 11:055062, 2009.
- [4] P. W. Anderson. *Phys. Rev*, 124:41, 1961.
- [5] S. Doniach. *Physica B & C*, 91:231, 1977.
- [6] H. Tsunetsugu, M. Sigrist, and K. Ueda. *Rev. Mod. Phys*, 69:809, 1997.
- [7] C.C. Yu and S.R. White. *Phys. Rev. Lett*, 71:3866, 1993.
- [8] R.M. Fye and D.J Scalapino. *Phys. Rev. Lett*, 65:3177, 1990.
- [9] J. C. Xavier. *Phys. Rev. B*, 68:134422, 2003.
- [10] C. Lacroix and M. Cyrot. *Phys. Rev. B*, 20:1969, 1979.
- [11] F. F. Assaad. *Phys. Rev. Lett*, 83:796, 1999.
- [12] Z. Wang, X.P. Li, and D.H. Lee. *Physica (Amsterdam)*, 199B-200B:463, 1994.
- [13] Z.P. Shi, R.R.P. Singh, M.P. Gelfand, and Z. Wang. *Phys. Rev. B*, 51:15630, 1995.
- [14] S. Paschen, T. Lühmann, S. Wirth, P. Gegenwart, O. Trovarelli, C. Geibel, F. Steglich, P. Coleman, and Q. Si. *Nature (London)*, 432:881, 2004.
- [15] H. Watanabe and M. Ogata. *Phys. Rev. Lett*, 99:136401, 2007.
- [16] N. Lanata, P. Barone, and M. Fabrizio. *Phys. Rev.B*, 78:155127, 2008.
- [17] L.C. Martin and F.F. Assaad. *Phys. Rev. Lett*, 101:066404, 2008.
- [18] L.C. Martin, M. Bercx, and F.F. Assaad. *Phys. Rev. B*, 82:245105, 2010.
- [19] J.C. Xavier and E. Dagotto. *Phys. Rev. Lett*, 100:146403, 2008.
- [20] Y. Liu, H. Li, G. Zhang, and L. Yu. *Phys. Rev. B*, 86:024526, 2012.

- 
- [21] F. Steglich, J. Aarts, W. Leike C. D. Bredl, D. E. M. W. Franz, and H. Schafer. *Phys. Rev. Lett*, 43:1892, 1976.
- [22] P. Flude and J. Keller. *Solid state Physics*, 41:1, 1988.
- [23] P. A. Lee, T. M. Rice, J. W. Serene, L. J. Sham, and J. W. Wilkins. *Comments Condens. Matt. Phys*, 12:99, 1986.
- [24] H. R. Ott. *Prog. Low Temp Phys*, 11:215, 1987.
- [25] W.J. de Haas, J. de Boer, and G. J. van den Berg. *Physica*, 1:1115, 1934.
- [26] A. M. Clogston, B. T. Mathias, M. Peter, H. J. Williams, E. Corenzwit, and R. C. Sherwood. *Phys. Rev*, 125:541, 1962.
- [27] M. Sarachik, E. Corenzwit, and L. D. Longinotti. *Phys. Rev*, 135:A1041, 1964.
- [28] A. Blandin and J. Friedel. *J. Phys. Radium*, 19:573, 1958.
- [29] J. R. Schrieffer and P. Wolff. *Phys. Rev*, 149:491, 1966.
- [30] B. Coqblin and J. R. Schrieffer. *Phys. Rev*, 185:847, 1969.
- [31] H. Von Löhneysen, A. Rosch, M. Vojta, and P. Wolfe. [arXiv.org/abs/cond-mat/0606317](https://arxiv.org/abs/cond-mat/0606317), 2007.
- [32] E. Miranda and V. Dobrosavljevic. *Rep. Prog. Phys*, 68:2337, 2005.
- [33] G. Stewart. *Rev. Mod. Phys*, 73:797, 2001.
- [34] C. Varma, Z. Nussinov, and W. Van saarlos. *Phys. Rep*, 361:267, 2002.
- [35] J. A. Hertz. *Phys. Rev. B*, 14:1165, 1976.
- [36] A. J. Millis. *Phys. Rev. B*, 48:7183, 1993.
- [37] T. Moriya. *Spin Fluctuations in Itinerant Electron Magnetism*. Springer and Berlin, 1985.
- [38] Q. Si, S. Rabello, K. Ingersent, and J. L. Smith. *Nature*, 413:804, 2001.
- [39] P. Coleman, C. Pépin, Q. Si, and R. Ramazashvili. *J. Phys. Cond. Matt*, 13:R723, 2001.
- [40] T. Senthil, M. Vojta, and S. Sachdev. *Phys. Rev. B*, 69:035111, 2004.
- [41] I. Paul, C. Pépin, and M. R. Norman. *Phys. Rev. Lett*, 98:026402, 2007.

- [42] F. M. Grosche, I. R. Walker, S. R. Julian, N D Mathur, D. M. Freye, and G. G. Lonzarich. *J. Phys. Condens. Matter*, 13:2845, 2001.
- [43] O. Stockert, E. Faulhaber, G. Zwicknagl, N. Stüßer, H. S. Jeevan, M. Deppe, R. Borth, R. KÜchler, M. Loewenhaupt, C. Geibel, and F. Steglich. *Phys. Rev. Lett*, 92:136401, 2004.
- [44] P. Gegenwart, Q. Si, and F. Steglich. *Nat. Phys*, 4:186, 2008.
- [45] N. Grewe and F. Steglich. *Handbook on the Physics and Chemistry of Rare Earths*, volume 14. Elsevier and Amsterdam, 1991.
- [46] H. V. Löhneyson, T. Pietrus, G. Portisch, A. Schröder H. G. Schlager, M. Sieck, and T. Trappamann. *Phys. Rev. Lett*, 72:3262, 1994.
- [47] C. L. Seaman, M. B. Maple, B. W. Le, and S. Ghamaty. *Phys. Rev. Lett*, 67:2882, 1991.
- [48] B. Andraka and G. R. Stewart. *Phys. Rev. B*, 47:3208, 1993.
- [49] B. Andraka and A. M. Tsvelik. *Phys. Rev. Lett*, 67:2886, 1991.
- [50] M. Sigrit and K. Ueda. *Rev. Mod. Phys*, 63:239, 1991.
- [51] D. Cox, M, and Maple. *Physics Today*, 482:32, 1995.
- [52] B. Maple, W. Fertig, A. Mota, L. DeLong, D. Wohlleben, and R. Fitzgerald. *Solid St. Commun*, 11:829, 1972.
- [53] N. D. Mathur, F. M. Grosche, S. R. Julian, I. R. Walker, D. M. Freye, R. K. W. Haemlwimmer, and G. G. Lonzarich. *Nature*, 394:39, 1998.
- [54] K. Miyake, S. Schmitt-Rink, and C. M. Varma. *Phys. Rev. B*, 34:6554, 1986.
- [55] Jozef Spalek. *Phys. Rev. B*, 38:208, 1988.
- [56] J. E. Hirsch. *Phys. Rev. Lett*, 54:1317, 1985.
- [57] B. B. Zhou, S. Misra, E. H. da Silva Neto, P. Aynajian, R. E. Baumbach, J. D. Thompson, E. D. Bauer, and A. Yazdani. *Nature Physics*, 2013.
- [58] J. Flouquet. *Progress in Low Temp. Physics*. Elsevier and Amsterdam 2005.
- [59] N. Metropolis, A. Rosenbluth, M. Rosenbluth, A. Teller, and E. Teller. *J. Chem. Phys*, 21:1087, 1953.
- [60] S. Sorella, G. Santoro, and F. Becca. *SISSA lecture notes on numerical methods for strongly correlated electrons*, [www.sissa.it/~sorella/Simulazioni.pdf](http://www.sissa.it/~sorella/Simulazioni.pdf).

- 
- [61] S. Sorella. *Phys. Rev. B*, 71:241103, 2005.
- [62] T. Kasuya. *Prog. Theo. Phys*, 16:45, 1956.
- [63] M.A. Ruderman and C. Kittel. *Phys. Rev*, 96:99, 1954.
- [64] K. Yosida. *Phys. Rev*, 106:893, 1957.
- [65] G. M. Zhang and L. Yu. *Phys. Rev. B*, 62:76, 2000.
- [66] S. Capponi and F. F. Assaad. *Phys. Rev. B*, 63:155114, 2001.
- [67] S. Sorella. *Phys. Rev. B*, 71:241103, 2005.
- [68] S. Sorella, G. B. Martins, F. Becca, C. Gazza, A. Parola L. Capriotti, and E. Dagotto. *Phys. Rev. Lett*, 88:117002, 2002.
- [69] L. Spanu, M. Lugas, F. Becca, and S. Sorella. *Phys. Rev. B*, 77:024510, 2008.
- [70] O. Bodensiek, R. Žitko, M. Vojta, M. Jarrell, and T. Pruschke. *Phys. Rev. Lett*, 110:146406, 2013.
- [71] B. Johansson. *Philos. Mag*, 30:469, 1974.
- [72] L. De Leo, M. Civelli, and G. Kotliar. *Phys. Rev. B*, 77:075107, 2008.
- [73] P. Coleman and A. H. Nevidomskyy. *Journal of Low Temperature Physics*, 161:182, 2010.
- [74] G. Martinez, J. R. Iglesias, C. Lacroix, and B. Coqblin. *Physica B*, 259:219, 1999.
- [75] S. Nakatsuji, Y. Machida, Y. Maeno, T. Tayama, T. Sakakibara, J. van Duijn, L. Balicas, J. N. Millican, R. T. Macaluso, and J. Y. Chan. *Phys. Rev. Lett*, 96:087204, 2006.
- [76] M. S. Kim, M. C. Bannett, and M. C. Aronson. *Phys. Rev. B*, 77:144425, 2008.
- [77] M. Neumann, J. Nyeki, B. Cowan, and J. Saunders. *Science*, 317:1356, 2007.
- [78] L. Isaev and I. Vekhter. *Phys. Rev. Lett*, 110:026403, 2013.
- [79] N. K. Sato, N. Aso, K. Miyake, R. Shiina, P. Thalmeier, G. Varelogiannis, C. Geibel, F. Steglich, P. Flude, and T. Komatsubara. *Nature*, 410:340, 2001.
- [80] J. R. Iglesias, C. Lacroix, and B. Coqblin. *Phys. Rev. B*, 56:11820, 1997.
- [81] F. López-Aguilar. *Phys. Rev. B*, 62:415, 2000.
- [82] A. E. Sikkema, I. Affleck, and S. R. White. *Phys. Rev. Lett*, 79:929, 1997.

- 
- [83] S. Moukouri and L. G. Caron. *Phys. Rev. B*, 54:12212, 1996.
- [84] E. Dagotto, T. Hotta, and A. Moreo. *Phys. Rep*, 344:1, 2001.
- [85] S. Yunoki and A. Moreo. *Phys. Rev. B*, 58:6403, 1998.
- [86] M.Z. Asadzadeh, F. Becca, and M. Fabrizio. *Phys. Rev. B*, 87:205144, 2013.
- [87] M.Z. Asadzadeh, F. Becca, and M. Fabrizio. *To be published*.

